The Destruction of Bars by Central Mass Concentrations

Juntai Shen & J. A. Sellwood

Department of Physics and Astronomy, Rutgers University, 136 Frelinghuysen Road, Piscataway, NJ 08854

shen@physics.rutgers.edu; sellwood@physics.rutgers.edu

ABSTRACT

More than two thirds of disk galaxies are barred to some degree. Many today harbor massive concentrations of gas in their centers, and some are known to possess supermassive black holes (SMBHs) and their associated stellar cusps. Previous theoretical work has suggested that a bar in a galaxy could be dissolved by the formation of a mass concentration in the center, although the precise mass and degree of central concentration required is not well-established. We report an extensive study of the effects of central masses on bars in high-quality N-body simulations of galaxies. We have varied the growth rate of the central mass, its final mass and degree of concentration to examine how these factors affect the evolution of the bar. Our main conclusions are: (1) Bars are more robust than previously thought. The central mass has to be as large as several percent of the disk mass to completely destroy the bar on a short timescale. (2) For a given mass, dense objects cause the greatest reduction in bar amplitude, while significantly more diffuse objects have a lesser effect. (3) The bar amplitude always decreases as the central mass is grown, and continues to decay thereafter on a cosmological time-scale. (4) The first phase of bar-weakening is due to the destruction by the CMC of lower-energy, bar-supporting orbits, while the second phase is a consequence of secular changes to the global potential which further diminish the number of bar-supporting orbits. We provide detailed phase-space and orbit analysis to support this suggestion.

Thus current masses of SMBHs are probably too small, even when dressed with a stellar cusp, to affect the bar in their host galaxies. The molecular gas concentrations found in some barred galaxies are also too diffuse to affect the amplitude of the bar significantly. These findings reconcile the apparent high percentage of barred galaxies with the presence of central massive concentrations, and have important implications for the formation and survival of bars in such galaxies.

Subject headings: black hole physics, stellar dynamics — galaxies: evolution — galaxies: ISM — galaxies: kinematics and dynamics — galaxies: nuclei — galaxies: structure

1. Introduction

Bars are one of the most prominent morphological features presented by disk galaxies; Eskridge et al. (2000) find that more than two thirds of disk galaxies are either strongly or weakly barred in the near-infrared band.

Central mass concentrations (CMCs) are also frequently found in galaxies of all types, including barred galaxies. A few examples of CMCs are:

- Large condensations of molecular gas with scales of $0.1 \sim 2$ kpc and masses of $10^7 \sim 10^9 M_\odot$ are found in the central regions (e.g. Sakamoto et al. 1999; Regan et al. 2001). They are particularly evident in barred galaxies, where they are believed to be created by bar-driven inflow (e.g. Athanassoula 1992; Heller & Shlosman 1994).

- Central supermassive black holes (SMBHs) seem to be a ubiquitous component in spiral galaxies as well as in ellipticals. Typical masses are in the range of $10^6 \sim 10^9 M_\odot$, and there is a loose correlation with bulge luminosity (Magorrian et al. 1998), suggesting the mass of the SMBH is roughly $0.006 M_{\mathrm{bulge}}$, where M_{bulge} is the mass of the bulge. Recent measurements with improved accuracy constrained the typical mass of a SMBH to be about $10^{-3} M_{\mathrm{bulge}}$ (Ferrarese & Merritt 2000; Gebhardt et al. 2000; Tremaine et al. 2002). Furthermore, a black hole is thought to be surrounded by a stellar cusp (Young 1980), which augments the effective mass of a SMBH for the purpose of large-scale morphological changes.

- Dense star clusters are found near the centers of many spiral galaxies (Carollo 2003; Walcher et al. 2003), which are young, very compact (a few to up to 20 pc) and relatively massive ($10^6 \sim 10^8 M_\odot$).

For the purposes of this paper, a CMC is any sufficiently large mass at the center of galaxy that is likely to have a dynamical effect on the evolution of its host galaxy. In other words we focus on the dynamical consequences of such objects regardless of their nature.

Studies of single-particle dynamics in rotating bar potentials with a CMC (Hasan & Norman 1990; Hasan, Pfenniger & Norman 1993), and some limited N-body simulations (see below) have given rise to a general belief that a CMC can weaken or dissolve the bar.

Yet CMCs appear to coexist with bars in many spiral galaxies. In order to determine whether this presents a genuine paradox, we need to know how massive a CMC is needed to destroy the bar completely and on what timescale.

The best way to address these questions is with fully self-consistent N-body simulations. Unfortunately, different papers in the literature give apparently discrepant results. The simulations by Norman, Sellwood & Hasan (1996) showed that a 5% mass can cause the bar to dissolve on a dynamical timescale. That by Friedli (1994), which included both stars and gas, indicated that objects with 2% of the disk mass could dissolve the bar on the time scale of about 1 Gyr. Hozumi & Hernquist (1998), who employed a 2-D self-consistent field (SCF) method, found that black holes with 0.5 to 1% of the total disk mass are sufficient to weaken the bar substantially within a few Gyrs. Berentzen et al. (1998) found, from a single experiment, that the gas inflow driven by a stellar bar concentrates a gas mass some 1.6% of that of the galaxy into the center, which causes the bar to decay on a timescale of 2 Gyrs. Bournaud & Combes (2002) also found that bars are very fragile.

There are a number of reasons to regard these results and their implications as tentative. First, the high frequency of bars in galaxies suggests they cannot be destroyed with any great efficiency (Miller 1996). Indeed, the massive gas content of the central regions of some barred galaxies (Sakamoto et al. 1999; Regan et al. 2001), as large as a few $10^9 M_\odot$ in some cases, suggest that the destruction of bars by CMCs is less efficient than claimed.

Second, large discrepancies between the different experimental results suggest possible numerical problems with the simulations or misunderstood implications. The simulations to study these processes are highly challenging numerically: there is a wide range of timescales on which the particles need to be integrated, and a large number of particles is also very important in order to make the mass of an individual particle much smaller than the central mass and to minimize Poisson noise.

Moreover, none of the previous studies presented a *systematic* exploration of the parameter space relevant to the evolution of bars. In particular, most restricted themselves to varying the mass of central objects, and unfortunately did not pay close attention to the "compactness" of the CMC, which we show here to be almost as important.

Studies of bar-forming mechanisms (Sellwood 2000) and secular evolution of barred galaxies are seriously hampered by our inadequate understanding of the influence of CMCs on the bar. The existence of CMCs in early stages of galaxies makes this problem even more urgent. There is mounting evidence to indicate that massive black holes grow very rapidly in their early stages, some reaching $\gtrsim 10^9 M_\odot$ at $4 \lesssim z \lesssim 6$ (Fan et al. 2001; Vestergaard 2004).

Our main motivation of this work is to verify (or otherwise) previous results, and to determine the timescale on which the bar is weakened by a CMC, the critical mass of the CMC which causes rapid bar dissolution, and other parameters vital to the bar-weakening process by CMCs. We have carried out a systematic investigation with extensive high-quality simulations. Our aim in this study, is not to attempt perfect realism, but rather to study the dynamics of bar destruction in isolation from other possible evolutionary behavior.

2. Model and Simulation Details

2.1. Model setup

In outline, our overall strategy is to first construct a model galaxy which is bar unstable. We follow its evolution until the bar rotates at nearly constant pattern speed (i.e. rotation rate) and with a roughly constant amplitude, in the absence of a CMC. Long after the bar has settled, we grow a CMC from zero to its final mass within a certain growth time, and study how the bar is weakened in response to the CMC growth. We learn how the bar is affected by some parameter, such as the growth time of the CMC, from a series of simulations as we change that parameter while keeping the rest fixed.

2.1.1. Self-consistent bar models

In this work we mainly study two initial bars formed in different ways, which we name weak and strong initial bars because of their relative strengths. We create the weak initial bar simply by evolving a Kuz'min-Toomre (K-T) disk, which has the surface density distribution

$$\Sigma(R) = \frac{M_{\mathrm{d}}}{2\pi a^2}\left(1 + \frac{R^2}{a^2}\right)^{-3/2}. \tag{1}$$

Here R is the cylindrical radius and a is a length scale. We select disk particles from a distribution function designed to yield the Toomre stability parameter $Q \simeq 1.5$ (Kalnajs 1976; Athanassoula & Sellwood 1986). We truncate the K-T disk at $R = 5a$, spread the particles vertically as the isothermal sheet with a locally-defined equilibrium vertical velocity dispersion, and embed it in the halo (see §2.1.3). The values of the parameters used in the initial setup are listed in Table 1.

We allow the model, which is globally unstable, to form a bar. Some time after the bar develops, the well-known buckling instability (Toomre 1966; Raha et al. 1991; Sellwood &

Wilkinson 1993) thickens the bar. After these events, we obtain a disk containing a long-lived bar having moderate strength, which we designate our weak initial bar.

In order to create a strong initial bar, we add fresh particles on circular orbits in the disk mid-plane to a similar weak bar model, which started from a slightly thicker initial disk, so that the buckling instability was milder. We adopt one of the addition rules described in Sellwood & Moore (1999), selecting the angular momentum J of each new particle from a Gaussian distribution with mean $\bar{J} = 1 + 0.0025t$ (in the units described in the next paragraph) and dispersion $\sigma_J = 0.5$ (also see Table 1); empirically, we find these parameters cause the bar to strengthen. This particle-adding process mimics the gradual growth of the disk in a simplified way.

We adopt a and M as our units of length and mass, respectively, and our time units are therefore dynamical times $\sqrt{a^3/GM}$. From here on all quantities are expressed in units such that $G = M = a = 1$ unless otherwise noted. These units can be scaled to physical values as desired; we adopt one possible scaling, choosing $M = 5 \times 10^{10} M_\odot$ and $a = 3$ kpc, which implies a unit of time of roughly 1.2×10^7yr.

2.1.2. Central Mass Concentrations

We mimic a CMC as a Plummer sphere for simplicity, i.e. its potential is given by:

$$\Phi_{\mathrm{CMC}}(r) = -\frac{GM_{\mathrm{CMC}}(t)}{\sqrt{r^2 + \epsilon_{\mathrm{CMC}}^2}}, \tag{2}$$

where $M_{\mathrm{CMC}}(t)$ is the CMC mass. We regard the scale-length of the CMC, ϵ_{CMC} (or softening length), as a physically interesting parameter, since it controls the compactness of the CMC. For example, we use a very small ϵ_{CMC} ($\sim$ a few pc, much less than the influence radius of a SMBH with about one percent of galactic mass) for a "hard" CMC to mimic a SMBH and relatively large ϵ_{CMC} ($\sim$ a few hundred pc) for a "soft" CMC to represent a massive gas concentration.

We grow the CMC by increasing its mass according to the relation

$$M_{\mathrm{CMC}}(t) = \begin{cases} 0 & \tau < 0, \\ M_{\mathrm{CMC}} \sin^2(\pi\tau/2) & 0 \le \tau \le 1, \\ M_{\mathrm{CMC}} & \tau > 1, \end{cases} \tag{3}$$

with $\tau = (t - t_{\mathrm{CMC}})/t_{\mathrm{grow}}$, for a CMC introduced at t_{CMC}. This sinusoidal time dependence is almost exactly the same as the cubic-type form adopted by Merritt & Quinlan (1998),

Hozumi & Hernquist (1998), and others. Note that in this work we hold ϵ_{CMC} fixed as the CMC mass is grown, in contrast to Norman et al. (1996) who decreased ϵ_{CMC} at fixed mass.

We adopt $t_{\mathrm{grow}} \gtrsim 50$ for most of our simulations. Even though t_{grow} may not be comparable to the rotational period of our initial bars (~ 30 or 50 time units), we regard this as adiabatic growth because t_{grow} is much longer than the orbital periods of particles near the disk center.

2.1.3. Halo component

We include a rigid halo in most of our simulations, having a potential of the form

$$\Phi_{\mathrm{halo}} = \frac{V_0^2}{2} \ln \left(1 + \frac{r^2}{c^2} \right).$$ (4)

This choice yields an asymptotically flat circular velocity of V_0 for $r \gg c$, with c being the "core radius." We choose a large core radius, $c = 30a$, and $V_0 = 0.7(GM/a)^{1/2}$.

We include this large-core halo as a rigid component instead of a "live" one represented by real particles, mainly for computational economy. In §4.3 we demonstrate that a live halo, with very similar potential to the rigid one, gives nearly same evolution in the bar-destruction process by CMCs. So we are assured that our results are not compromised by this simplification.

2.2. Numerical methods

In most of our simulations, we employ the 3-D cylindrical polar grid-based N-body code described in detail by Sellwood & Valluri (1997). We solve separately for the three components of the gravitational acceleration and for the potential of the mass distribution using Fast Fourier Transforms (FFTs) in the vertical and azimuthal directions and by direct convolution in the radial direction. The gravitational field at a distance d from a unit mass follows the standard (Plummer sphere) softened potential $\Phi(d) = -G/\sqrt{d^2 + \epsilon^2}$ where the softening length, ϵ, is a constant. We generally employ more than one million particles in our runs; most numerical parameters adopted are listed in Table 1.

We advance the motion of each particle using simple time-centered leap-frog in Cartesian coordinates. A fixed time step for all particles is impractical because of the wide range of time-scales, and we vary the time step length in two separate ways. Our fundamental time step, Δt, defines the interval between successive determinations of the gravitational field

of all the particles. We divide the computation volume into 4 zones and advance particles in the outer zones using longer time steps; the spherical zone boundaries are at $r = 0.6$, $r = 1.0$, and $r = 2.0$, and time steps are doubled in each successive zone. Contributions to the gravitational field from the outer zones to accelerations near the center are computed from time-interpolated estimates of the slowly-changing outer mass distribution (Sellwood 1985).

We also implement "guard shells" (see Appendix A) around a CMC in which the most rapidly moving particles are integrated on shorter time steps; the shortest step can be as small as $\Delta t/2^9$ for hard CMCs. Since the gravitational field inside the tiny guard shells is dominated by the CMC, we do not update the field of the mobile particles during these sub-steps.

For test runs with a live halo, we use a hybrid PM scheme (Appendix B of Sellwood 2003), in which the self-gravity of the disk is computed on a high-resolution cylindrical polar grid while that of the halo is computed using a surface harmonic expansion on a spherical grid.

The code conserves total energy and angular momentum to a satisfactory degree in these challenging experiments. In our fiducial run (§3.1), $|\Delta E/E| \approx 0.5\%$ and $|\Delta L_z/L_z| \approx 0.9\%$ over 100 time units, once CMC growth has ceased.

2.3. Measure of bar strength

Our estimator of bar strength is

$$A(t) = \frac{1}{N} \left| \sum_{j=1}^{N} \exp[2i\theta_j] \right| \tag{5}$$

which is the relative amplitude of the bisymmetric ($m = 2$) Fourier component of the mass density averaged over certain inner radial range where the bar dominates. Here θ_j is the coordinate of each of the N particles in the radial range $0.5 < R < 2$ in the simulation at time t. Our strong initial bar has a greater radial extent, and therefore $|A|$ underestimates its true amplitude, but we have held this radial range fixed for both bars in order to minimize differences between the quantities measured; we are most interested in changes to $|A|$ and not its absolute value.

We also measure the *ellipticity*, $e \equiv 1 - b/a$, where a and b are respectively the semi-major and semiminor axes of the bar. We estimate e by fitting iso-density contours using the Image Reduction and Analysis Facility (IRAF) to smooth projected density profiles con-

structed from the particle distribution using an adaptive kernel scheme (Silverman 1986). Observers generally use the maximum value of ellipticity as the measure of bar amplitude (e.g. Laurikainen, Salo & Rautiainen 2002). However, the maximum ellipticity in our simulations sometimes fluctuates due to complications such as spiral waves. We therefore use the ellipticity measured at certain reasonably-chosen fixed semi-major axis, which yields a measure with much smaller fluctuations. Laurikainen, Salo & Rautiainen (2002) have shown that the ellipticity of a bar correlates quite well with the maximum relative tangential force Q_b (Buta & Block 2001), another indicator of bar strength, in the bar region.

We find that the two estimators of bar strength, A and e, behave in similar ways as the CMC grows (see §3.1). We therefore generally rely on A only, since it is much easier to calculate from an N-body simulation.

3. Results

We first present the result of a fiducial run in §3.1, then describe results from our systematic exploration of parameter space; checks of our simulations are discussed in §4.

3.1. A fiducial run

Figure 1 illustrates how a typical barred model reacts as a CMC with mass $M_{\mathrm{CMC}} = 0.02M_{\mathrm{d}}$ and scale-length $\epsilon_{\mathrm{CMC}} = 0.001$ is grown according to Eq. (3) with $t_{\mathrm{grow}} = 50$. Figure 1(a) shows snapshots of particle positions and Figure 1(b) the corresponding iso-density contours, obtained by smoothing every particle with an adaptive kernel.

This experiment starts with the strong initial bar, which rotates steadily with period ~ 50 at constant amplitude. The CMC starts to grow at the first time shown ($t = 700$) in Figure 1, and its mass rises to $0.02M_{\mathrm{d}}$ by $t = 750$. The bar is weakened by the CMC, but not destroyed, and retains a moderate strength to the last time shown.

The heavy solid line in Figure 2 represents $A(t)$, the evolution of the amplitude defined in (5), for our fiducial run. The bar weakens rapidly as the CMC mass rises, but the bar amplitude decreases much more slowly after $t = 750$. Figure 2 also shows the time evolution of the ellipticity e. The striking similarity of the overall evolutionary trends of these two estimators assures us that A is indeed a good bar-strength indicator.

The scale-length of this CMC is roughly two orders of magnitude smaller than the influence radius ($r_h = GM_{\mathrm{BH}}/\sigma^2 \sim 0.12$; here $\sigma \sim 0.4$ is the flat central value of the velocity

dispersion before the CMC is grown) of a SMBH with the same mass, so this CMC can be regarded as a SMBH-type object. However, its mass is of course much greater than typical SMBH masses in spiral galaxies, which are about $10^{-3}M_{\mathrm{bulge}}$ (Ferrarese & Merritt 2000; Gebhardt et al. 2000; Tremaine et al. 2002). Our intention here is to demonstrate that a bar can survive even with such an extraordinarily massive hard CMC.

3.2.   Bar amplitude A vs. t_{grow}

Figure 3 shows how the bar amplitude evolves for different t_{grow}; the uppermost line indicates that the bar amplitude stays roughly constant in a comparison run with no central mass. The oscillations visible around $t = 800$ and $t = 1200$ are due to interference by spiral features just outside the bar region that have different pattern speeds from that of the bar. They do not cause any lasting change to the bar amplitude.

The other lines show that bar is rapidly weakened as the central mass grows. Shortly after the CMC mass reaches its maximum value, the bar amplitude A decays on a much longer timescale for this fixed central mass. The transition between the two trends becomes less sharp for large t_{grow} ($\gtrsim 200$). Thus, we confirm, as found in previous work (e.g. Norman et al. 1996; Hozumi & Hernquist 1998), that that t_{grow} is not very important in determining the final bar amplitude long after CMC growth, even when the mass is introduced impulsively and not adiabatically. We use $t_{\mathrm{grow}} = 50$ in all subsequent work.

3.3.   Bar amplitude A vs. ϵ_{CMC}

The importance of the compactness (i.e. the scale-length) of CMCs is explicitly shown in Figure 4. The bar amplitude in Figure 4 is measured at a fixed time, long (250 time units) after the CMC starts to grow. The final $M_{\mathrm{CMC}} = 0.02M_{\mathrm{d}}$ for all runs in Figure 4. The solid and dashed curves represent experiments with weak and strong initial bars, respectively. Both types of initial bar show a similar trend: *hard CMCs are much more destructive to bars than are softer ones.* Note that the trend of bar amplitude with ϵ_{CMC} is flattening out as the CMC becomes very hard.

The typical sizes of molecular gas concentrations in the centers of galaxies range from a few hundred parsecs to 2 kpc or so (e.g. Sakamoto et al. 1999, Regan et al. 2001), which corresponds to $0.1 \sim 1$ in our simulation units. Thus diffuse gaseous CMCs cause much less damage to bars than would equally massive but significantly more compact counterparts such as SMBHs.

3.4.   Bar amplitude A vs. M_{CMC}

Figure 5 shows the final bar amplitude at the end of simulations (~ 6 Gyrs after CMC growth) as a function of M_{CMC}, for both types of initial bar. This figure indicates that the final bar amplitude decreases continuously as M_{CMC} is increased, and again we see that hard CMCs cause much more damage to bars than do soft ones (also see Figure 4). For both initial bars, we find that the bar is effectively destroyed when the mass of a hard ($\epsilon_{\mathrm{CMC}} = 0.001$) CMC is greater than 4% or 5% of M_{d}, whereas soft ($\epsilon_{\mathrm{CMC}} = 0.1$) CMCs as massive as $\sim 0.1 M_{\mathrm{d}}$ do not destroy the bar within ~ 6 Gyr (500 time units).

4.   Parameter Tests and Numerical Checks

These simulations are technically very challenging. Here we report a few of our many tests to check that our main results and conclusions are reliable. Some of our findings might account for the discrepant results obtained by other groups.

4.1.   Numerical parameter tests

Figure 6 presents tests (for the weak initial bar) of the number of particles N, grid size and particle softening, respectively. We have conducted a similar suite of tests for the strong initial bar, with similar results. The amplitude difference shown in the top panel for the two experiments with different N starts and remains very small (it is hard to achieve precisely the same bar parameters). There is a mild dependence on particle softening, slightly more pronounced for the strong initial bar, which we discuss below. These figures confirm that variations of particle number and grid size by a factor of two or more around our adopted values make negligible difference to our main results.

4.2.   Time step

We do, however, find that the evolution is sensitive to the adopted time step Δt, and one obtains more rapid, but erroneous, bar destruction by CMCs if the orbit integration is not handled with sufficient care.

If a single time step is used over the whole simulation domain, Δt needs to be as small as $10^{-5} \sim 10^{-4}$ to ensure that all particles are integrated accurately (see Appendix A), for a typical simulation containing a hard central mass with $M_{\mathrm{CMC}} = 0.02 M_{\mathrm{d}}$ and $\epsilon_{\mathrm{CMC}} = 0.001$.

Time steps this short are, of course, too expensive for practical use, which is the reason for the multiple zones and guard shell schemes described above.

Figure 7 shows the effect of changing the time step while all other parameters are held fixed. When no guard shells are employed, the bar amplitude at a fixed time becomes weaker as the time step is increased; there is no indication of convergence even for very small Δt. The bar amplitude is always greater when guard shells are employed, and is less sensitive to the particular choice of the basic Δt, since we divide it even more finely as Δt is increased. Even with guard shells, the final amplitude does increase mildly as the time step is reduced.

Since the severity of the time-step problem is greater for harder and more massive CMCs, it requires great care to determine the threshold for bar destruction.

4.3. Live halo tests

Figure 8 shows, for one case, that the bar amplitude evolution is hardly affected when the rigid halo is replaced by a similar live pseudo-isothermal halo with a large core resembling our rigid form (Eq. 4). Thus, our approximation of a rigid halo appears to be adequate.

While not a parameter test, we report here that a *dense* or *cuspy* live halo stimulates the growth of a bar, as noted by Debattista & Sellwood (2000) and discussed in more detail by Athanassoula & Misiriotis (2002) and Athanassoula (2003). Thus, a bar in a denser or cuspy halo is *even harder* to destroy, which underscores one of our main conclusions that bars are very robust.

4.4. Relation to other work

We are unable to understand all discrepancies with other experiments in the literature because many authors give insufficient information. We believe the parameters adopted by Norman et al. (1996) were adequate, and their results are largely consistent with ours.

We suspect inadequately short time steps could be a factor in accounting for the rapid bar decay claimed by some groups. For example, the shortest time step (0.4 Myr) used in Bournaud & Combes (2002) is equivalent to ~ 0.033 in our units, which our Figure 7 suggests is dangerously long.

But an inadequate time step may not be able to account for all the discrepancies. For example, Hozumi & Hernquist (1998) used a timestep $\Delta t = 0.005$ which should be adequate for $\epsilon_{\rm CMC} = 0.01$, but they found the bar to be quite fragile, inconsistent with our findings here.

We speculate that the difference might be due to the SCF (self-consistent field) simulation method they used, in which the gravitational field is computed from a rather low-order expansion in some set of basis functions. The method therefore raises a severe restriction on the complexity of shapes which their models could support. In particular such simulations may be unable to sustain a shape which is axisymmetric near the center while remaining non-axisymmetric in the outer parts, which might spuriously hasten the decay of bars.

5.   The Mechanism of Bar Dissolution by a CMC

A naïve explanation for the robustness of a bar against the central mass is that the orbits of most bar-supporting particles are little affected by the introduction of a light, dense central mass. This is because most bar-supporting orbits are loops that naturally tend to avoid the center of the bar due to the Coriolis force in a rotating frame (Sparke & Sellwood 1987; Hasan & Norman 1990; Sellwood & Wilkinson 1993; etc.). Contopoulos has designated this main family of bar-supporting orbits as x_1 orbits (see Contopoulos & Grosbøl 1989 for a review), but they are also sometimes described as B-orbits.

A more careful examination of Figure 3 reveals an intriguing phenomenon: the bar is generally weakened in two phases, divided by the time at which the CMC mass growth stops, which are easily distinguishable unless $t_{\rm grow}$ is extremely long (< 200). The first phase, which coincides with the CMC mass-growing period, is clearly controlled by $t_{\rm grow}$, except when it is very abrupt. Thus the response is effectively instantaneous because typical dynamical times of particles near the CMC are short in comparison with $t_{\rm grow}$. The second phase of bar weakening is on a much longer time scale ($\gtrsim 0.5$ Hubble time) and begins right after the period of CMC mass growth. Why is the bar weakened by the CMC in two distinct rates?

We suggest that the first phase of bar weakening is due mainly to the rapid scattering of x_1 particles with lower energies.[1] To support this suggestion, we present a study of orbits in the mid-plane ($z = 0$) of the bar.

One of the more powerful tools of orbit analysis is the surface of section (SOS) which can be constructed at any accessible energy. We adopt Cartesian coordinates in the rotating frame of the bar, with the major axis of the bar aligned with the x-axis, and integrate the orbits of test particles in a steadily rotating bar potential from some moment in the

---

[1]In a potential which rotates steadily at the rate Ω_p, energy is not conserved, but the Jacobi constant $E_J = E - \mathbf{\Omega_p} \cdot \mathbf{L} = \frac{1}{2}|\dot{\mathbf{r}}|^2 + \left(\Phi - \frac{1}{2}\Omega_p^2 R^2\right)$ is constant along on an orbit (Binney & Tremaine 1987). In this paper we loosely refer to the Jacobi constant E_J as the energy.

simulation. A SOS records the values of $(y, \dot{y})$ for a number of orbits all having the same energy, each time they cross the minor $(y-)$ axis with $\dot{x} < 0$. Particles in prograde motion in the frame of the bar have $y > 0$ when $\dot{x} < 0$, and particles in retrograde motion have $y < 0$ when $\dot{x} < 0$. An invariant curve, a series of points all lying on a closed curve in the SOS, is produced by a regular orbit that conserves a second integral in addition to the energy. Irregular, or chaotic, orbits conserve only one integral (E_J) and fill an area in this plane. The adopted energy of the SOS determines the maximum possible excursion, $y_{\max}$, on the bar minor-axis, which is the parameter we prefer to specify.

Figure 9 shows the SOS at two energies for the potential of the rotating bar at $t = 700$ before the CMC is grown. The series of nested invariant curves on the left arises from the retrograde (x_4) orbit family, which is not very eccentric even in this strongly non-axisymmetric potential. Because of their round shape, x_4 orbits do not support the bar and a self-consistent bar can contain rather little mass moving on orbits of this family.

The other series of nested invariant curves on the right of Figure 9 is of much greater importance. These regular prograde orbits are members of the x_1 family, and are widely believed to form the backbone of the bar. Figure 10(a) shows three examples of x_1 orbits selected from Figure 9(a), showing clearly that many particles on lower-energy x_1 orbits pass very close to the center; such orbits will be strongly affected by the introduction of even a low-mass, but dense, CMC. Regular x_1 orbits selected from the higher-energy SOS (Figure 9b), on the other hand, are larger (Figure 10b) and generally avoid the central region.

5.1. CMC growth phase

Figure 11 shows how the SOS at lower energies changes as the CMC in our fiducial run grows, corresponding to the first phase of bar weakening.[2] The breakdown of the large regular areas once occupied by the x_1 family is very striking. More and more bar-supporting particles become chaotic, as the growing central mass affects orbits that pass at ever increasing distances. Since chaotic orbits tend to have more nearly round long-time average shapes, it is clear that the bar is weakened in this phase because many regular bar-supporting orbits become chaotic.

Since the orbital periods of particles near the center are much shorter than t_{grow}, low-

---

[2] It should be emphasized that these Figures show the orbit structure in an assumed steady potential taken from the simulations at a number of different times. In reality, the gradual growth of the CMC causes a continuously changing potential.

energy orbits adjust essentially instantly to the new potential and the rate of change of bar amplitude tracks the CMC growth.

5.2. Structural adjustment

As the orbits of particles change, the global potential of the system evolves secularly, an effect that continues even after the CMC has reached its final mass. This structural adjustment is illustrated in Figure 12 for the fiducial run ($\epsilon_{\mathrm{CMC}} = 0.001$, $M_{\mathrm{CMC}} = 0.02M_{\mathrm{d}}$), which shows the slow evolution after t_{grow}.

The SOS at $y_{\mathrm{max}} = 1.4$ keeps evolving even after the CMC has reached full mass at $t = 750$. The Figure clearly shows that the area occupied by regular x_1 orbits at this lower-energy gradually diminishes and the x_2 orbit family, which does not support bar, becomes increasingly important among the prograde orbits at this energy level. The potential of the system also tends to favor x_1 orbits that are somewhat fatter in shape (Figure 13) at higher energies, since the once-strong bar has now been weakened.

Based on Figure 3, this structural adjustment happens on a very long timescale, $\gtrsim 0.5$ Hubble time. However, there is no reason to expect that the rate of this second-phase bar-weakening should remain constant over long time, in fact it becomes slightly slower during the course of our simulation (Figure 3). We also notice that the second phase bar decay rate is somewhat slower for the weak initial bar than for the strong initial bar, suggesting that the rate of secular structural change differs from case to case.

Note that this second phase of bar weakening could not be observed in studies of single particle dynamics in a rigid potential. It happens because the global potential evolves *self-consistently*, which requires an N-body simulation. Furthermore, we find that the area occupied by regular x_1 orbits shrinks rapidly for $M_{\mathrm{CMC}} \gtrsim 0.04M_{\mathrm{d}}$ when the potential is allowed to evolve, which could be achieved only by further increases in M_{CMC} if the bar strength is fixed (also see Hasan & Norman 1990).

5.3. Discussion of dissolution mechanisms

We find that two-phase bar destruction occurs only for compact CMCs of modest mass ($\lesssim 0.03M_{\mathrm{d}}$). A more massive CMC causes a larger fraction of x_1 orbits to become chaotic in the first phase, causing the second-phase structural adjustment to also happen very rapidly. Thus the self-consistent bar can no longer withstand the effect of the massive CMC and starts to dissolve. This idea may explain why the critical mass is about the same for both

strong and weak initial bars.

The fact that harder (more compact) CMCs cause more damage to bars than do softer (more diffuse) ones can also be explained qualitatively in our picture. The weaker forces from a soft CMC might be expected to introduce less chaos. This expectation is suported by the evidence in Figure 14, which compares the SOS for orbits of similar size in the presence of hard and soft CMCs. Figure 14(a) shows the SOS at $y_{max} = 1.2$ at $t = 800$ for the fiducial run with a hard ($\epsilon_{CMC} = 0.001$) CMC, while Figure 14(b) shows the same for a very diffuse ($\epsilon_{CMC} = 0.1$) CMC. The area of x_1 orbit family in Figure 14(b) is much larger than the corresponding region in Figure 14(a); similar SOS plots at other energies also show the same result. This is in agreement with the finding by Gerhard & Binney (1985) that the chaotic region in the SOS increases as the central mass is hardened.

Our picture may also be able to account for the erroneously faster bar decay resulting from inaccurate orbit integration (cf. §4.2). If a bar-supporting x_1 orbit is not followed very accurately as it approaches a CMC, values of integrals may change for numerical reasons, and a particle on a regular x_1 orbit could become chaotic. The enhanced loss of x_1 particles will lead to structural adjustment, making the inverse of this change, a chaotic orbit converting to a regular one, less likely. Thus such errors can only accelerate bar decay.

Figure 3 also shows that the bar amplitude at the end of CMC growth does not have the same value for the different t_{grow}, implying that secular structural change may have started the moment the CMC starts to grow.

Figure 6(c) showed a mild dependence of the final bar amplitude on particle softening, indicating that the decay rate in the second-phase is very slightly accelerated as softening is decreased. A slight increase in the rate of collisional relaxation is the most natural explanation but we stress that the effect is very minor even though the softening length changes by a factor of five. Such a weak dependence indicates that the models are indeed almost collisionless.

5.4. Is 2-D SOS an adequate tool for 3-D potentials?

Since 3-D orbit dynamics is complicated and very difficult to visualize, we do not wish to give a detailed discussion here. The preceding discussion concerned only those orbits confined to the $z = 0$ plane of the 3-D potential. This could be misleading, since many cases are known (e.g. Pfenniger 1984) where 2-D orbits are irregular while 3-D orbits, with projected shapes very similar to those in 2-D, may be regular. We therefore need to show that allowing 3-D motion does not change our arguments, especially in regard to the importance

of chaos.

The SOS in Figure 11(a), with no CMC, is a nice example of a strong bar that is supported by a large contribution from regular 2-D x_1 orbits, yet it was constructed from a 3-D bar. It therefore seems likely that the main bar-supporting orbits are not drastically altered when 3-D motion is allowed. Pfenniger & Friedli (1991) show that x_1-like orbits in 3-D are generally 2:2:1 resonant, that is they bob up and down about the mid-plane twice for each turn around the center in the rotating frame of the bar. Skokos, Patsis & Athanassoula (2002a,b) give a more comprehensive discussion. Since these orbits are simple 3-D generalizations of the x_1 orbit family that sustains 2-D bars, we expect the essentials of the phase space structure we find to carry over to 3-D bars.

We also need to show, however, that the evidence for chaos in our 2-D SOS is in fact accompanied by chaos in the full 3-D potential. In order to address this issue, and to complement our 2-D SOS study, we have carried out a Floquet analysis (Binney & Tremaine 1987). The existence of chaos is indicated by a positive Lyapunov exponent, which is defined as the *e*-folding divergence rate of two orbits starting with an infinitesimal separation in phase space. However, Valluri & Merritt (2000) show that Lyapunov exponents in stellar systems are not good predictors of regular or chaotic orbits, and suggest that a more practical criterion is whether the exponential divergence *continues* until the phase-space separations reach the system size.

As an example, Figure 15 shows the evolution of phase-space separation from a very small value for three orbits; the left-hand panel (a) shows the case when motion continues to be confined to the $z = 0$ plane, while the right-hand panel (b) shows cases in which full 3-D motion is allowed. The latter orbits start with the same $(x, y, z = 0)$ position, but move away from the mid-plane because the potential is not perfectly reflection symmetric. The two orbits in each panel for which the separation quickly reaches the system size are clearly chaotic while the orbit for which the separation remains at some value much smaller than the system size for a long time (~ 5 Gyr) is regular, according to the criterion proposed by Valluri & Merritt (2000). Thus for these three examples, at least, the (ir)regular nature is unchanged when 3-D motion is permitted.

In order to know whether a region that appears to be chaotic in 2-D remains fully, or mostly, chaotic when 3-D motion is allowed, we examine the phase-space separation of many pairs of orbits started at random in the region in question. We focus on two 3-D potentials at $t = 740$ and $t = 1200$, since both show large areas of chaos at some energy in the 2-D SOS plots (i.e. Figure 11(e) for $E_J = -0.6385$ at $t = 740$ and Figure 12(f) for $E_J = -0.5164$ at $t = 1200$). For 500 orbits, we choose the initial y at random from the range $-0.15 < y < 0.6$ for $t = 740$ and $-0.1 < y < 0.5$ for $t = 1200$, the initial $x = 0$, and the initial z is one of

five values between $z = \pm 0.2$. For velocities, we select V_x, V_y and V_z randomly to satisfy the selected E_J. From the criterion for a chaotic orbit described above (Figure 15), we find that about 90% of our randomly-chosen orbits are chaotic for $E_J = -0.6385$ at $t = 740$ and about 80% are chaotic for $E_J = -0.5164$ at $t = 1200$.

Thus this 3-D test confirms that most of the realistic 3-D orbits are chaotic, consistent with expectation of the 2-D SOS results. We therefore contend that a 2-D SOS indeed provides a simplified, yet useful, way to picture the underlying 3-D orbital structure in our study.

6.   Discussion

The experiments described here are rather artificial. We simply grow central masses in a pre-existing bar in order to learn how the bar is affected by CMCs having a range of properties. Our intention was to isolate and understand a single aspect of the dynamics, with as few complications as possible. Despite this, and other limitations, it may be reasonable to apply our main results to real galaxies.

6.1.   Limitations

We have restricted our simulations to collisionless stellar systems only, and have not attempted to include gas. We justify this mainly because simulations with gas are much more complicated and we have shown that it requires great care to get even the simpler collisionless results right. The forced inflow of gas is of considerable importance, and star formation, feedback, etc., will also affect the accumulation of gas near the center. However, gas mass fractions in galaxies today are thought to be modest, and the mass accumulations in the centers of bars appear not to be large enough to destroy the bars (as we discuss next); thus our approximation of treating all mobile material as if it were collisionless may capture most of the essential physics relevant to bar survival.

We have not included a bulge component in our models, largely because it would increase the number of parameters; we leave a study that includes realistic bulges for future work. Our results therefore apply most directly to small-bulge galaxies (late-type spirals). While SMBHs are associated directly with bulges, and not with disks, other types of CMCs are found in late-type galaxies. However, we do not expect the bar dissolution behavior to be substantially affected by the introduction of a modest bulge component because bulges are relatively diffuse objects. Even if the bulge density profile has an inner cusp of slope $r^{-\alpha}$,

the enclosed mass rises as $r^{3-\alpha}$ from the center, and therefore only a tiny fraction of the bulge mass will behave as a hard CMC.

We have studied two bars with different strengths and found consistent results. But the exact properties of a CMC to dissolve a bar may also depend on other details of the initial bar in host galaxies. For example, one might expect long slender bars to be more fragile than short stubby bars (also see Hasan & Norman 1990). The pattern speed might also affect the bar dissolution process, since Teuben & Sanders (1985) showed that dynamically slow bars are supported by different orbit families than are fast bars. However, it is hard to vary the bar pattern speed only while keeping other properties of the bar unchanged in a self-consistent study. In fact, the pattern speed and length of the bar appear to be closely related (Aguerri, Debattista & Corsini 2003).

It may be more appropriate to express the critical CMC mass as a fraction of the bar mass ($M_{\rm bar}$), since the outer disk presumably has little effect on the dynamics near the center of a bar. Unfortunately we found this impractical, as an accurate measure of $M_{\rm bar}$ alone requires us to separate the bar from the other components, which is hard to do – both for simulations and for real galaxies.

6.2. Implications

We have shown that the timescale for bar destruction depends on the mass of the CMC and that SMBH-like hard CMCs cause much more damage to bars than do soft ones. The critical SMBH mass to destroy bars on short timescale is about 4% or 5% of the disk mass for the bars used in our study. Ferrarese & Merritt (2000), Gebhardt et al. (2000), and Tremaine et al. (2002) estimated the mass of SMBHs found in many galaxies to be $\sim 10^{-3}$ of the *bulge* mass, and bulges are generally less luminous (e.g. Palunas & Williams 2000), and probably less massive, than the disk, except for rare cases. Thus SMBHs in galaxies are much less than this critical value and are therefore too small to pose a significant threat to the survival of bars today. For the same reason, central dense star clusters in some galaxies (Carollo 2003; Walcher et al. 2003) are also incapable of dissolving bars.

Our finding that bars are more robust than previously thought eliminates any possible paradox presented by the coexistence of SMBHs and gas concentrations in the centers of barred galaxies. It is widely believed that bars drive gas into the central regions (e.g. Athanassoula 1992), yet our findings indicate they should be able to survive such massive gas accumulations. Sakamoto et al. (1999) and Regan et al. (2001) detected much greater concentrations of molecular gas in barred galaxies than in unbarred ones. This is the op-

posite of what would be expected from rapid bar destruction by central gas concentrations, since greater accumulations would be observed in unbarred (*but previously barred*) galaxies, provided the gas concentration survives for some time.

Das et al. (2003) find an inverse correlation between the deprojected bar ellipticity (e) and the ratio of the dynamical mass within the bulge to that within the bar radius (f_{mc}) in a small sample of 13 nearby barred galaxies taken from the BIMA SONG survey. They argue that f_{mc} is a good indicator, although not a direct measure, of the central mass concentration, and they further suggest that the correlation with e may be the consequence of the bar dissolution by CMCs.

Their correlation needs to be confirmed in a larger sample. In particular, 11 of the 13 sample members are in the range of $0.3 < e < 0.62$, while only two have small ellipticities and essentially set the "tightness" of their inverse correlation. If we regard the two small-e galaxies as unreliable, because of uncertainties in deprojection (Barnes & Sellwood 2003), the inverse correlation between e and f_{mc} is rather loose.

If indeed real, the correlation would provide an important constraint on the bar weakening process by CMCs. For example, the modest diffuse CMCs they report can not cause *rapid* bar destruction ($\lesssim$ a couple of Gyrs), otherwise most bars should have been destroyed already. To avoid this conclusion, one would require bars to be rejuvenated in a special way, e.g. strong bars must reform in galaxies with smaller CMCs and vice versa. On the other hand, the correlation does not rule out our finding of slow bar dissolution; bars are weakened to differing extents, more by a large CMC and less by a small counterpart, and then survive at their weakened amplitude for a long time. Detailed predictions are impossible, however, because we currently lack a coherent picture of when, and in what sequence, bars and CMCs formed.

Our results suggest it is unlikely that large fractions of bulges are formed by bar dissolution, because the CMCs observed in galaxies today do not destroy bars. However, the bar weakening process does add some disk material to bulges, since those orbits which become chaotic because of the presence of the CMC fill a more nearly spherical volume near the center of the bar. Chaotic orbits which were quite elongated before the introduction of the CMC will contribute to the bulge density to a radius several times that of the usual sphere of influence of a SMBH. Furthermore, such a process might be more important in young galaxies when disks/bars were smaller and CMCs could have been proportionately more massive.

CMCs do not, of course, offer the only means to destroy or weaken bars. In fact, we have shown that neither realistic SMBHs nor diffuse molecular gas clouds can dissolve bars

with any great efficiency. There are other ways to weaken and destroy bars more efficiently than by growing a CMC. Bars can be destroyed in minor mergers (Berentzen et al. 2003 and references therein). Also Sellwood & Moore (1999) found that ongoing spiral activity in the outer disk triggered by newly formed "cold" material accreted onto the disk, which is not included in our present simulations, could either complete the destruction of the bar or cause it to grow again; buckling also weakens bars (e.g. Raha et al. 1991).

Our problem is similar to the question of whether a SMBH destroys the large-scale triaxiality of a typical elliptical galaxy. As these objects, which are believed to lack significant figure rotation, are supported mostly by box orbits and not by tubes, as in our case, the dynamics is quite different, yet it is interesting that the survival of triaxiality in this case is also not yet settled. Holley-Bockelmann et al. (2002) found that triaxiality may be long-lived even with a SMBH as massive as $0.01M_{\mathrm{galaxy}}$, while Merritt & Quinlan (1998) found that SMBHs with $0.003M_{\mathrm{galaxy}}$ are able to destroy large-scale triaxiality within a Hubble time. Further investigations in this area would also seem to be warranted.

7.   Conclusions

We have conducted a systematic study of the effects of central massive concentrations (CMCs) on bars using high-quality N-body simulations. We have experimented with both strong and weak initial bars and a wide range of physical parameters of CMCs, such as the final mass, scale-length and mass growth time t_{grow} etc. We have demonstrated that our main findings are insensitive to most numerical parameters in our simulation, and shown that the time step requires special care particularly for the cases with compact CMCs.

We find that, for a given mass, compact CMCs (such as supermassive black holes) are more destructive to bars than are more diffuse ones (such as molecular gas clouds in many galactic centers). We have shown that the former are more efficient scatterers of bar-supporting x_1 orbits that pass close to the center, therefore decrease the number of regular x_1 orbits and increase the size of the chaotic region in phase space.

A bar is generally weakened by a CMC in two connected phases. The bar strength decreases rapidly as the central mass grows due to the rapid scattering of stars on lower-energy bar-supporting x_1 orbits as they pass close to the CMC. The time scale for this first phase is therefore the orbital period of the stars in the bar or the growth rate of the central mass, whichever is the longer. The bar continues to decay thereafter on a cosmological timescale (e.g. $\gtrsim 0.5$ Hubble time for a compact CMC with $0.02M_{\mathrm{d}}$). The second phase reflects slow evolution of the gravitational potential causing a gradual loss of bar-supporting

x_1 orbits.

Bars are more robust against CMCs than previously thought: the central object, even for the most destructive SMBH-like CMCs, has to be as massive as a few percent of the disk mass to destroy a bar completely within a Hubble time. On the other hand, diffuse CMCs need a tremendous amount of mass ($> 0.1 M_\mathrm{d}$) to achieve the same effect.

Our findings clearly show that neither typical SMBHs in spirals ($M_\mathrm{CMC} \sim 10^{-3} M_\mathrm{Bulge}$) nor typical central molecular gas concentrations (mass $M_\mathrm{CMC} \lesssim$ a few percent of M_d, scale $R \sim$ a few hundred pcs) can have any significant weakening effect on the bar within a Hubble time – the former are generally not massive enough, whereas the latter are too diffuse. Thus, our results can naturally account for the coexistence of CMCs and bars in many spiral galaxies.

REFERENCES

Aguerri, J. A. L., Debattista, V. P., & Corsini, E. M. 2003, MNRAS, 338, 465

Athanassoula, E. 1992, MNRAS, 259, 345

————. 2003, MNRAS, 341, 1179

Athanassoula, E., & Misiriotis, A. 2002, MNRAS, 330, 35

Athanassoula, E. & Sellwood, J. A. 1986, MNRAS, 221, 213

Barnes, E. I., & Sellwood, J. A. 2003, ApJ, 125, 1164

Berentzen, I., Athanassoula, E., Heller, C. H., & Fricke, K. J. 2003, MNRAS, 341, 343

Berentzen, I., Heller, C. H., Shlosman, I., & Fricke, K. J. 1998, MNRAS, 300, 49

Binney, J., & Tremaine, S. 1987, Galactic Dynamics (Princeton: Princeton Univ. Press)

Bournaud, F., & Combes, F. 2002, A&A, 392, 83

Buta, R., & Block, D. L. 2001, ApJ, 550, 243

Carollo, C. M. 2003, Carnegie Observatories Astrophysics Series, Vol. 1: Coevolution of Black Holes and Galaxies, ed. L. C. Ho (Cambridge: Cambridge Univ. Press)

Contopoulos, G. & Grosbøl, P. 1989, A&A Rev., 1, 261

Das, M., Teuben, P. J., Vogel, S. N., Regan, M. W., Sheth, K., Harris, A. I., & Jefferys, W. H. 2003, ApJ, 582, 190

Debattista, V. P., & Sellwood, J. A. 2000, ApJ, 543, 704

Eskridge, P. B., et al. 2000, AJ, 119, 536

Fan, X. et al. 2001, AJ, 122, 2833

Ferrarese, L., & Merritt, D. 2000, ApJ, 539, L9

Friedli, D. 1994, in Mass-Transfer Induced Activity in Galaxies, ed. I. Shlosman (Cambridge: Cambridge Univ. Press), p. 268

Gebhardt, K. et al. 2000, ApJ, 539, L13

Gerhard, O. E., & Binney, J. 1985, MNRAS, 216, 467

Hasan, H., & Norman, C. 1990, ApJ, 361, 69

Hasan, H., Pfenniger, D., & Norman, C. A. 1993, ApJ, 409, 91

Heller, C. H. & Shlosman, I. 1994, ApJ, 424, 84

Holley-Bockelmann, K., Mihos, C. J., Sigurdsson, S., Hernquist, L., & Norman, C. 2002, ApJ, 567, 817

Hozumi, S., & Hernquist, L. 1998, astro-ph/9806002

Kalnajs, A. J. 1976, ApJ, 205, 751

Laurikainen, E., Salo, H., & Rautiainen, P. 2002, MNRAS, 331, 880

Magorrian, J. et al. 1998, AJ, 115, 2285

Merritt, D., & Quinlan, G. 1998, ApJ, 498, 625

Miller, R. H. 1996, in "Barred galaxies" ASP Conference Series, Volume 91 (San Francisco: Astronomical Society of the Pacific) ed. by R. Buta, D. A. Crocker and B. G. Elmegreen, p. 569

Norman, C. A., Sellwood, J. A., & Hasan, H. 1996, ApJ, 462, 114

Palunas, P., & Williams, T. B., 2000, ApJ, 120, 2884

Pfenniger, D. 1984, A&A, 134, 373

Pfenniger, D., & Friedli, D. 1991, A&A, 252, 75

Raha, N., Sellwood, J. A., James, R. A., & Kahn, F. D. 1991, Nature, 352, 411

Regan, M. W., et al. , ApJ, 2001, 561, 218

Sakamoto, K., Okamura, S. K., Ishizuki, S., & Scoville, N. Z. 1999, ApJ, 525, 691

Skokos, C., Patis, P. A., & Athanassoula, E. 2002a, MNRAS, 333, 847

——, 2002b, MNRAS, 333, 861

Sellwood, J. A. 1985, MNRAS, 217, 127

Sellwood, J. A. 2000, in "Dynamics of Galaxies: from the Early Universe to the Present", 15th IAP meeting held in Paris, France, July 9-13, 1999, Eds.: Francoise Combes, Gary A. Mamon, and Vassilis Charmandaris, ASP Conference Series, Vol. 197, p. 3

——. 2003, ApJ, 587, 638

Sellwood, J. A. & Evans, N. W. 2001, ApJ, 546, 176

Sellwood, J. A., & Moore, E. M. 1999, ApJ, 510, 125

Sellwood, J. A., & Valluri, M. 1997, MNRAS, 287, 124

Sellwood, J. A., & Wilkinson, A. 1993, Rep. Prog. Phys., 56, 173

Silverman B. W. 1986, Density Estimation for Statistics and Data Analysis (London: Chapman and Hall)

Sparke, L. S., & Sellwood, J. A. 1987, MNRAS, 225, 653

Teuben, P. J., & Sanders, R. H. 1985, MNRAS, 212, 257

Toomre, A. 1966, in Geophysical Fluid Dynamics, notes on the 1966 Summer Study Program at the Woods Hole Oceanographic Institution, ref. no. 66-46, p. 111

Toomre, A. 1981, in The Structure and Evolution of Normal Galaxies, ed. S. M. Fall & D. Lynden-Bell (Cambridge: Cambridge University Press), 111

Tremaine, S. et al. 2002, ApJ, 574, 740

Valluri, M., & Merritt, D. 2000, in "The Chaotic Universe", Proceedings of the Second ICRA Network Workshop, Advanced Series in Astrophysics and Cosmology, vol.10, Edited by V. G. Gurzadyan and R. Ruffini, World Scientific, p.229. also see astro-ph/9909403

Vestergaard, M. 2004, ApJ, in press, astro-ph/0309521

Walcher, C. J. et al. 2003, Carnegie Observatories Astrophysics Series, Vol. 1: Coevolution of Black Holes and Galaxies, ed. L. C. Ho (Pasadena: Carnegie Observatories, http://www.ociw.edu/ociw/symposia/series/symposium1/proceedings.html

Young, P. 1980, ApJ, 242, 1232

A. Guard shells scheme

We have devised the following "guard shells" scheme in order to improve the accuracy of orbit integration when particles experience strong acceleration near a compact central mass. We divide the volume around the CMC into many concentric shells and successively halve the time step for particles in each shell as they approach the CMC (Figure 16). Since accelerations in this small region are dominated by the field of the CMC, we integrate the orbit for these sub-timesteps in a fixed field, and update the self-consistent part from the bar and the disk at the basic time step interval Δt.

In the region dominated by the CMC, the orbital period τ of a test particle moving on a circular orbit satisfies

$$|F_r| = \frac{d\Phi_{\mathrm{CMC}}}{dr} = \frac{r\,GM_{\mathrm{CMC}}}{(r^2 + \epsilon_{\mathrm{CMC}}^2)^{3/2}} = \left(\frac{2\pi}{\tau}\right)^2 r,$$

so

$$\tau(r) = 2\pi\sqrt{\frac{(r^2 + \epsilon_{\mathrm{CMC}}^2)^{3/2}}{GM_{\mathrm{CMC}}}}.$$

We choose the outermost guard radius r_{max} so that $\tau(r_1 = r_{\mathrm{max}})/\Delta t$ is $\gtrsim 100$. Particles inside r_{max}, which have shorter periods, require finer time steps. We adopt time steps in adjacent shells that differ by a factor of two, making it appropriate to require $\tau(r_{i+1}) = \tau(r_i)/2$. Since $\tau \propto r^{3/2}$ (if $r \gg \epsilon_{\mathrm{CMC}}$), the ratio of adjacent guard radii is

$$\frac{r_{i+1}}{r_i} = \left[\frac{\tau(r_{i+1})}{\tau(r_i)}\right]^{2/3} = \left(\frac{1}{2}\right)^{2/3} \approx 0.63.$$

We keep this ratio constant for simplicity, although this is somewhat over-conservative for $r \sim \epsilon_{\mathrm{CMC}}$.

The shortest possible orbital period is

$$\tau_{\mathrm{min}} = \tau(r = 0) = 2\pi\frac{\epsilon_{\mathrm{CMC}}^{3/2}}{\sqrt{GM_{\mathrm{CMC}}}}.$$

The number of guard shells (n), or the boundary of the innermost zone (r_{min}), is determined so that $\tau_{\mathrm{min}}/(\Delta t/2^n) \gtrsim 50$ say, which we find to be adequate.

Table 1. Summary of the model setup

Quantity	Strong initial bar	Weak initial bar[a]
Numerical Parameters		
Initial number of particles ..	2.0×10^6	1.2×10^6
Final number of particles ...	2.8×10^6	
Grid size (R, ϕ, z)	$55 \times 64 \times 375$	$55 \times 64 \times 375$
Vertical plane spacing	0.02	0.02
Grid boundaries (R, z)	$(20.0, \pm 3.74)$	$(20.0, \pm 3.74)$
Particle softening length	0.02	0.05
Time step Δt_0 — w/o CMC	0.04	0.04
Time step Δt — w/ CMC ..	0.01	0.01
Number of guard shells with the fiducial CMC	9	9
Outermost guard radius r_{max}[b]	0.127	0.127
Innermost guard radius r_{min}	0.003	0.003
Initial Disk		
Toomre Q	1.5	1.5
RMS vertical thickness	0.13	0.05
Truncation radius	5	5
Fixed halo		
V_0	0.7	0.7
Core radius c	30	30
Accretion rule[c]		
Particles added per Δt_0	80	
Accretion rule	Gaussian in J	
	$\bar{J} = 1 + 0.0025t$, $\sigma_J = 0.5$	

[a]No particles added in the weak initial bar case

[b]See Appendix A for more details

[c]See Sellwood & Moore (1999) for more details
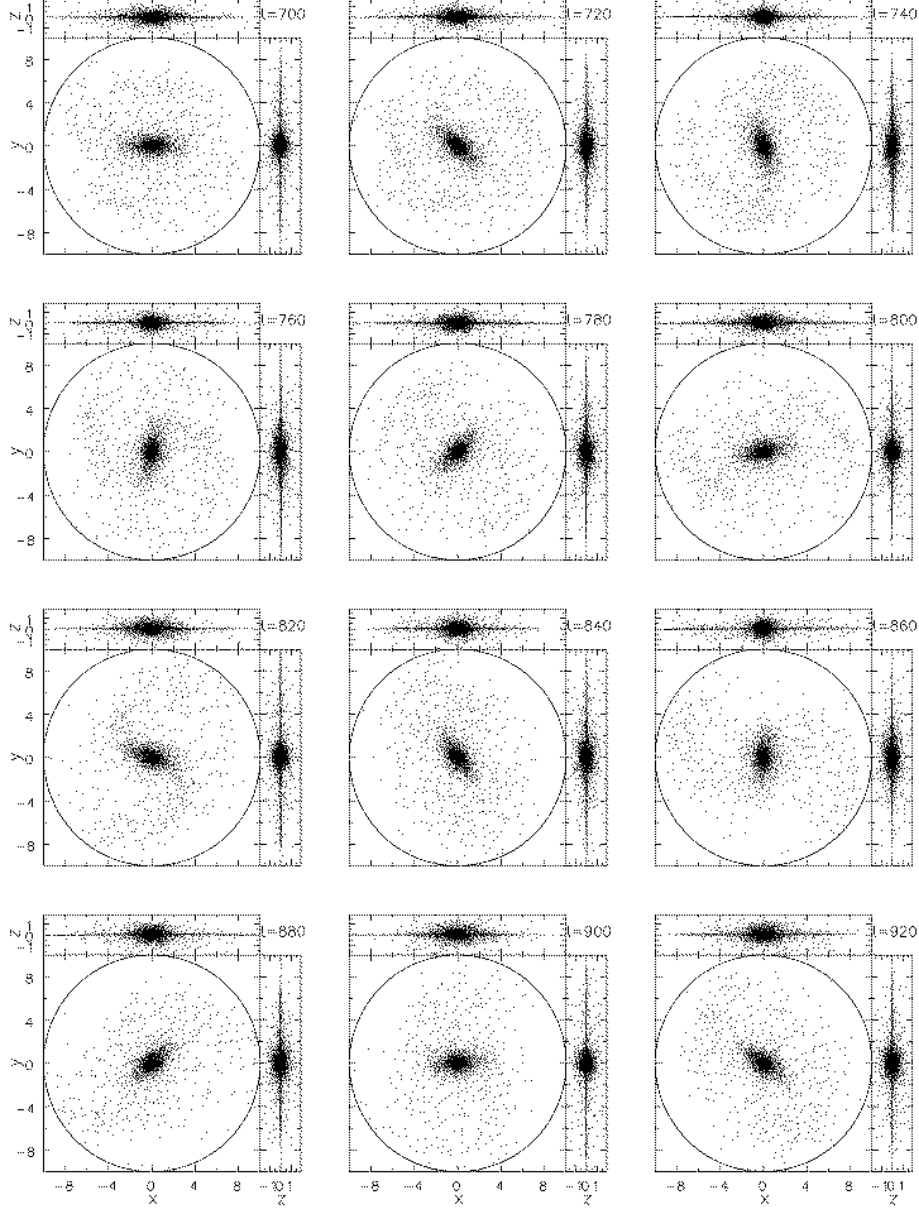
Fig. 1.— (a) Snapshots of particle positions showing the evolution of the fiducial model. Only about 1 in 500 particles is shown. The compact CMC with $M_{CMC} = 0.02$ is grown from $t = 700$ to 750 according to Eq. (3). The vertical extent of the grid in the simulation is about twice that shown in the figure.
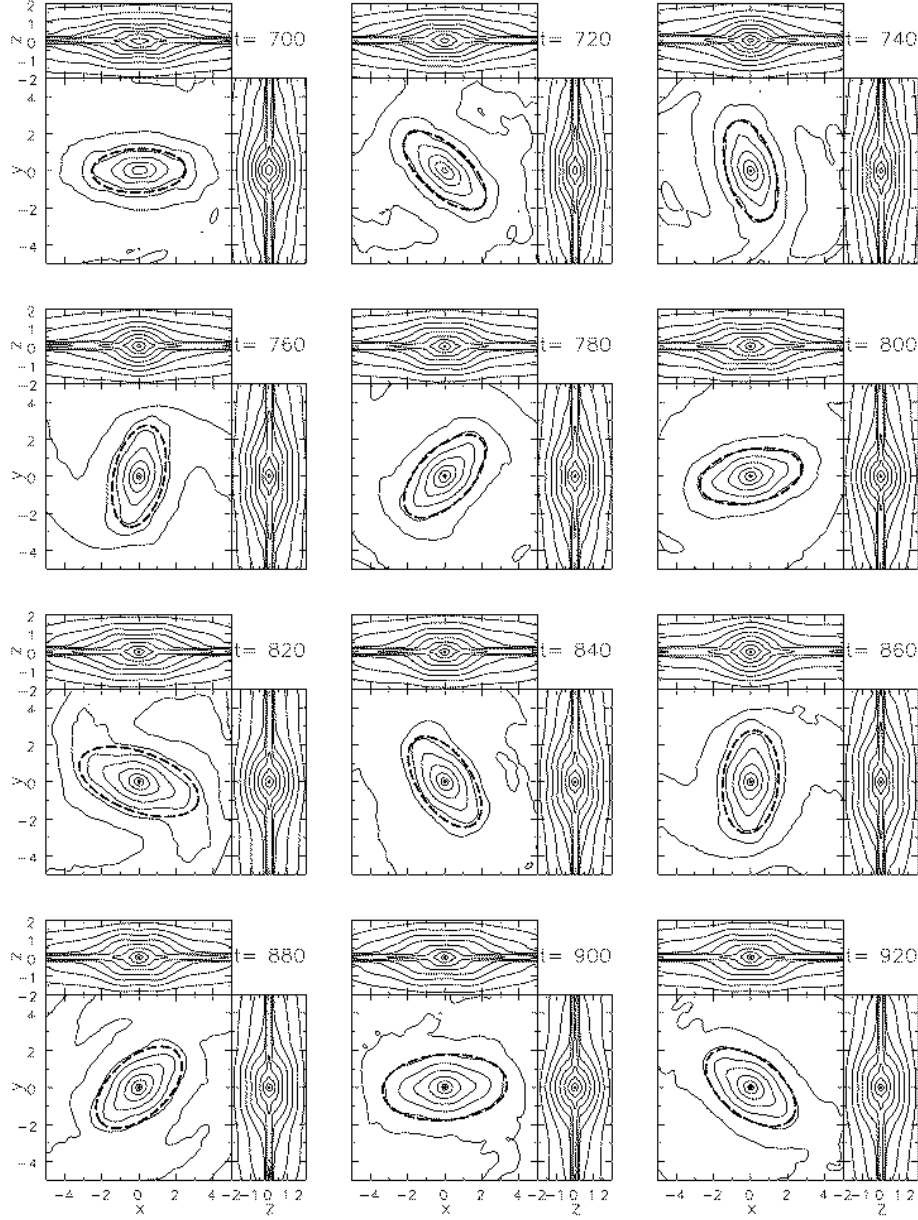
Fig. 1.— (b) Contours of projected density, obtained by smoothing the particles with an adaptive kernel, at the same moments as shown in (a). Note that the scale is not the same. The dashed ellipse in each panel is the best fit ellipse with the greatest ellipticity, resulting from the task `ellipse` in IRAF. The best-fit ellipse appears to match the neighboring density contours quite well. Contours are separated by a constant ratio of $10^{0.4}$ (one magnitude in projected density).
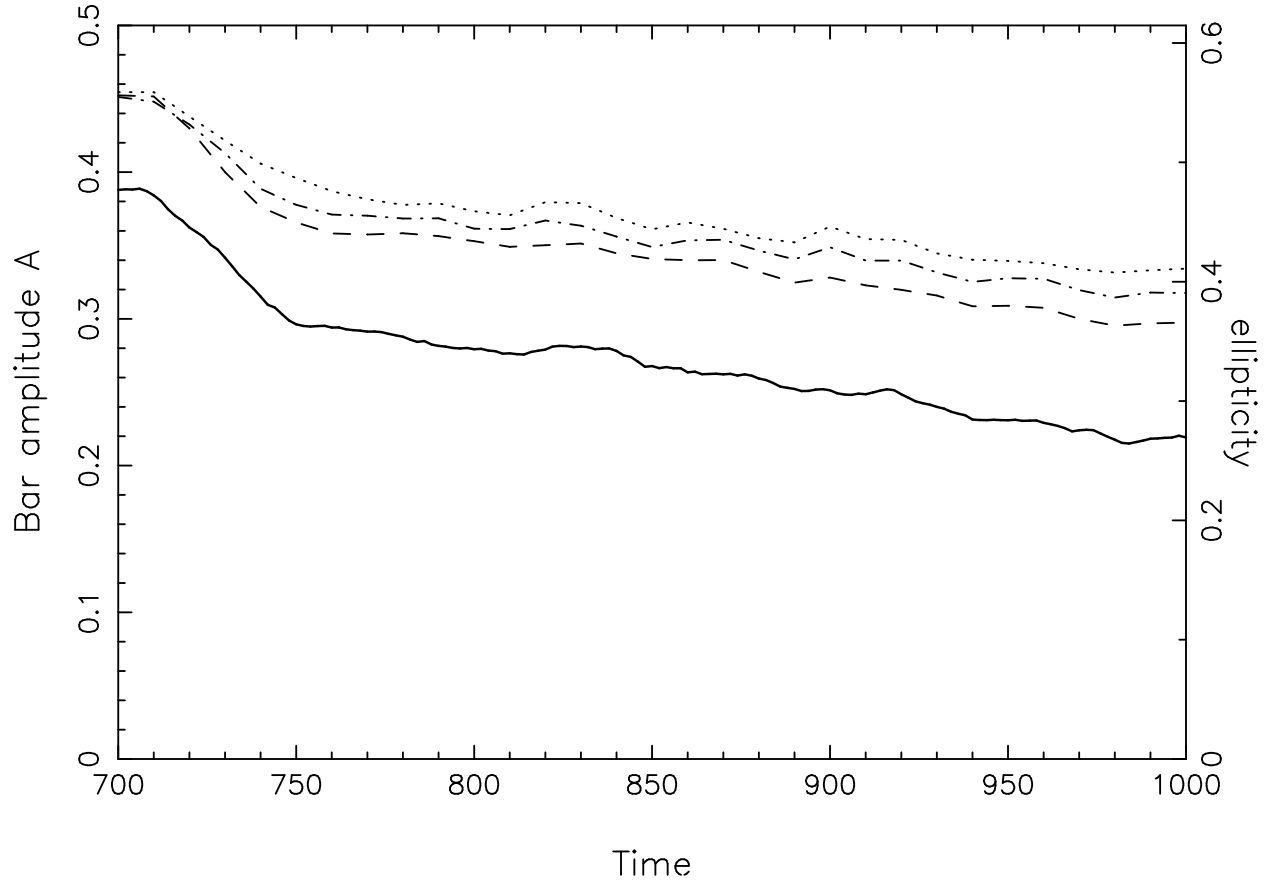
Fig. 2.— The time evolution of the bar amplitude A (heavy solid line) and ellipticity e measured at SMA=2.0, 1.75 and 1.5 (dotted, dash-dotted and dashed curves), respectively.
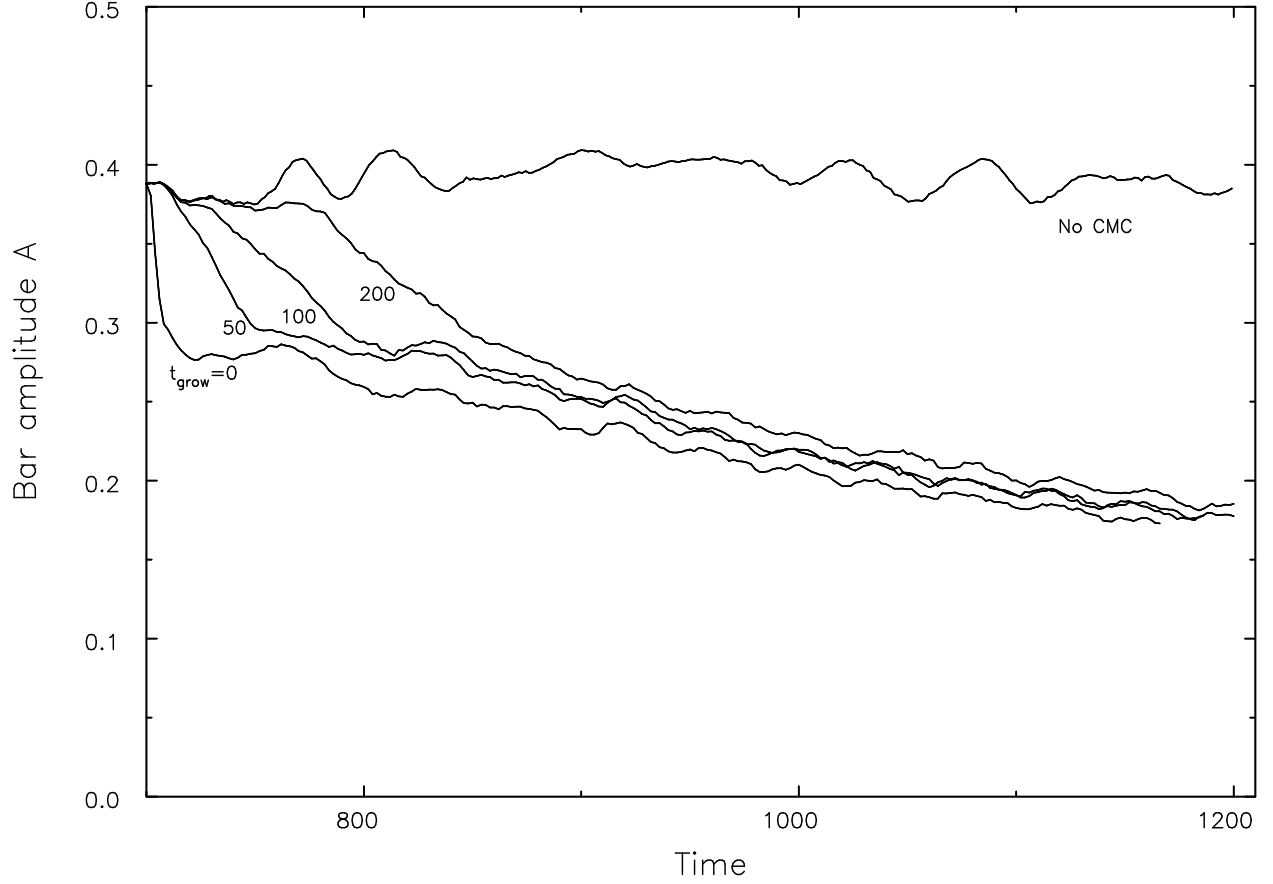
Fig. 3.— Evolution of bar amplitude A for runs with the same CMC ($M_{\mathrm{CMC}} = 0.02M_{\mathrm{d}}$, $\epsilon_{\mathrm{CMC}} = 0.001$) but grown at different rates. The uppermost curve is a comparison run with no CMC, the others are marked by the value of t_{grow}. The pattern speed of this initial bar is about 50 time units.
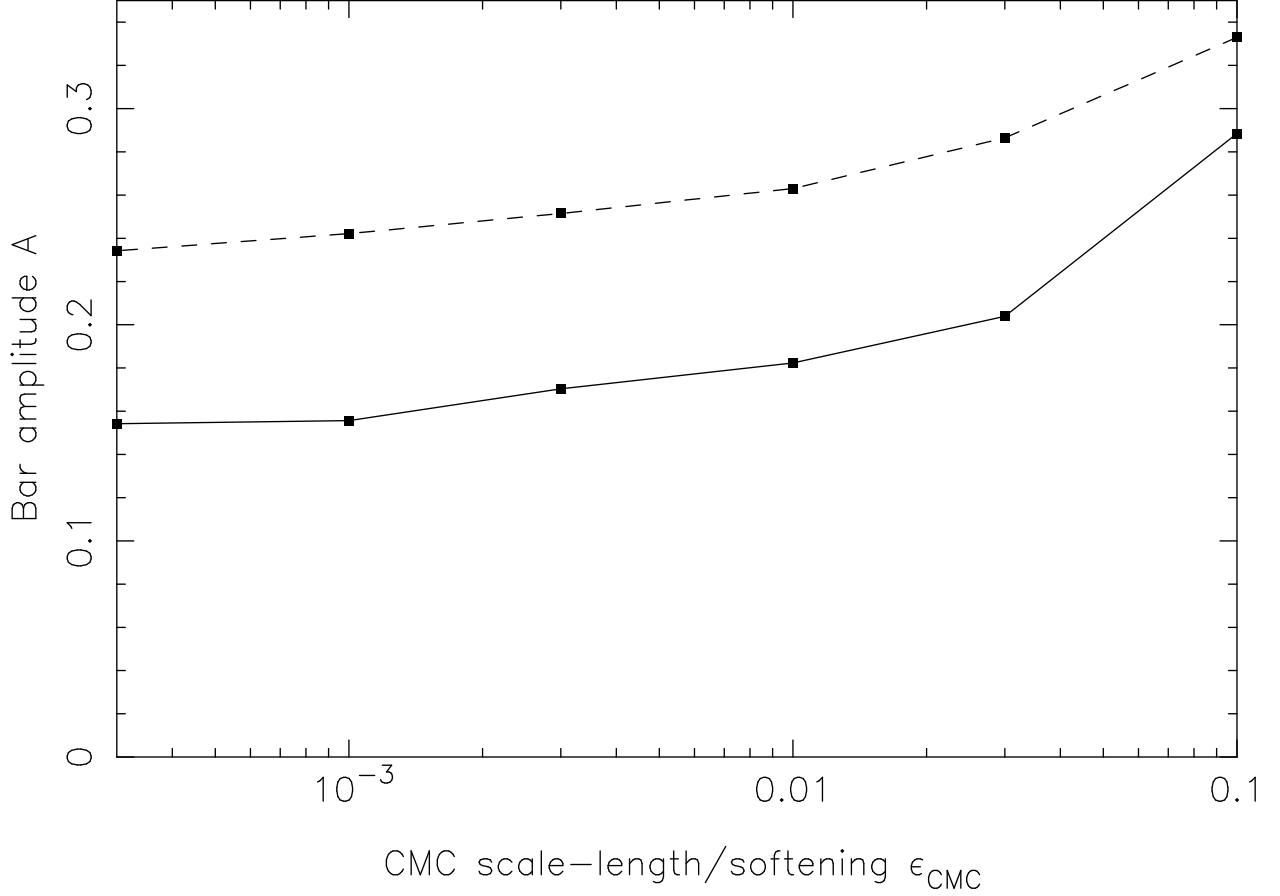
Fig. 4.— The bar amplitude A, measured 250 time units after the central mass starts to grow, as a function of ϵ_{CMC}, with other CMC parameters fixed ($M_{\mathrm{CMC}} = 0.02 M_{\mathrm{d}}$). The solid and dashed curves show results for the weak and strong initial bars, respectively. The trend in both curves is similar: denser CMCs cause significantly more damage to the bar, but both curves flatten as ϵ_{CMC} decreases.
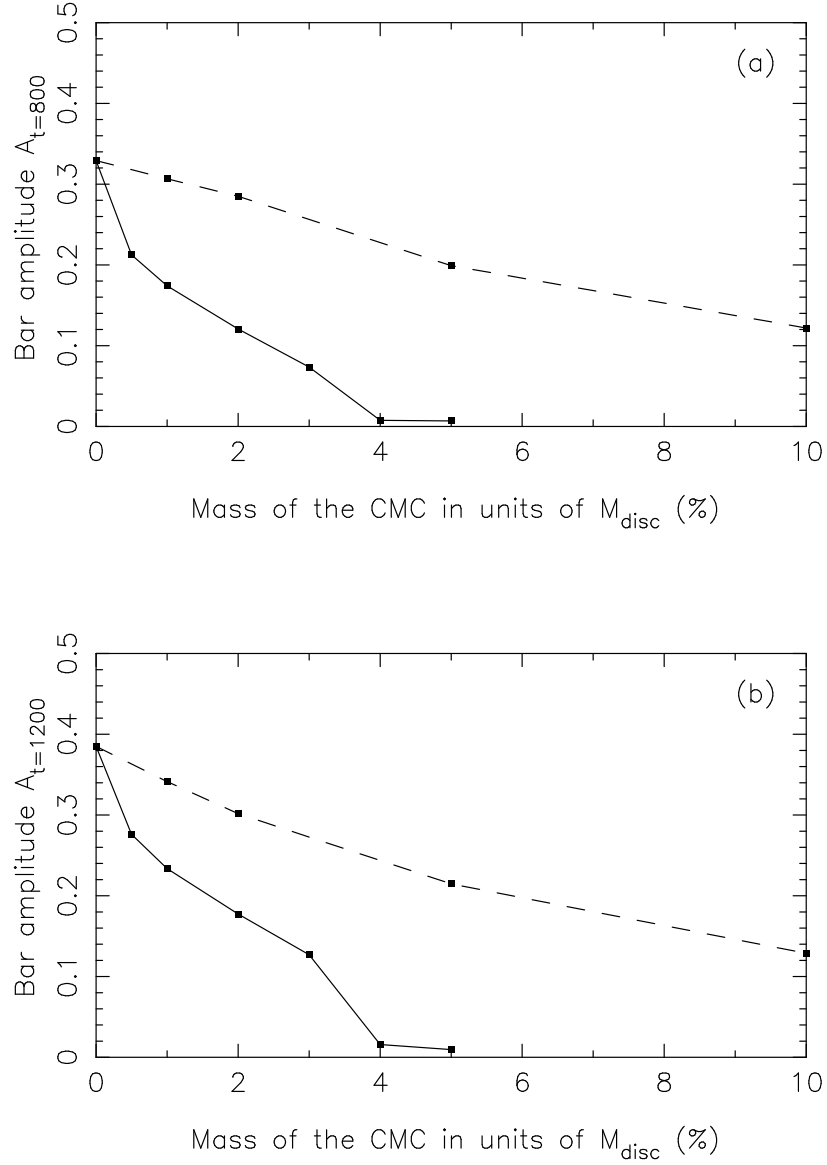
Fig. 5.— (a) The final amplitude of the weak initial bar as a function of M_{CMC}, with other CMC parameters fixed. The solid and dashed curves represent the runs with a hard ($\epsilon_{\mathrm{CMC}} = 0.001$) and soft CMC ($\epsilon_{\mathrm{CMC}} = 0.1$), respectively. (b) As for (a), but for the strong initial bar. The final bar amplitude decreases continuously as M_{CMC} is increased, and hard CMCs always cause significantly more damage to the bar than do soft ones. The bar is destroyed on short time scales by a hard CMC with a mass a few percent M_{d}, but the mass of a soft CMC needs to be $\gtrsim 0.1 M_{\mathrm{d}}$.
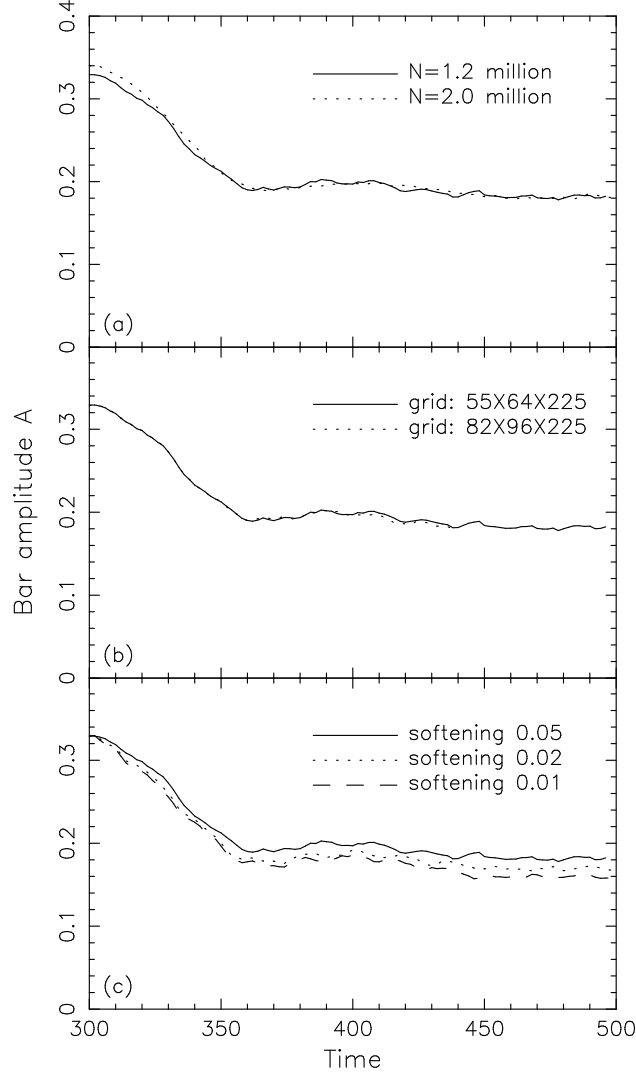
Fig. 6.— Tests to show that the bar-weakening behavior is little affected when we vary the numerical parameters by a factor of two or more around the adopted values. These tests are for the weak initial bar, with the same CMC parameters ($M_{CMC} = 0.02M_d$, $\epsilon_{CMC} = 0.003$ and $t_{grow} = 50$). (a) Two runs with different numbers of particles. Note that the initial bars in these two runs start with slightly different A. (b) Two with different grid sizes. The test run with a much finer grid yields almost exactly same result as the run with our standard grid. (c) Tests with different particle softening from 0.05 to 0.01, with other physical parameters unchanged.
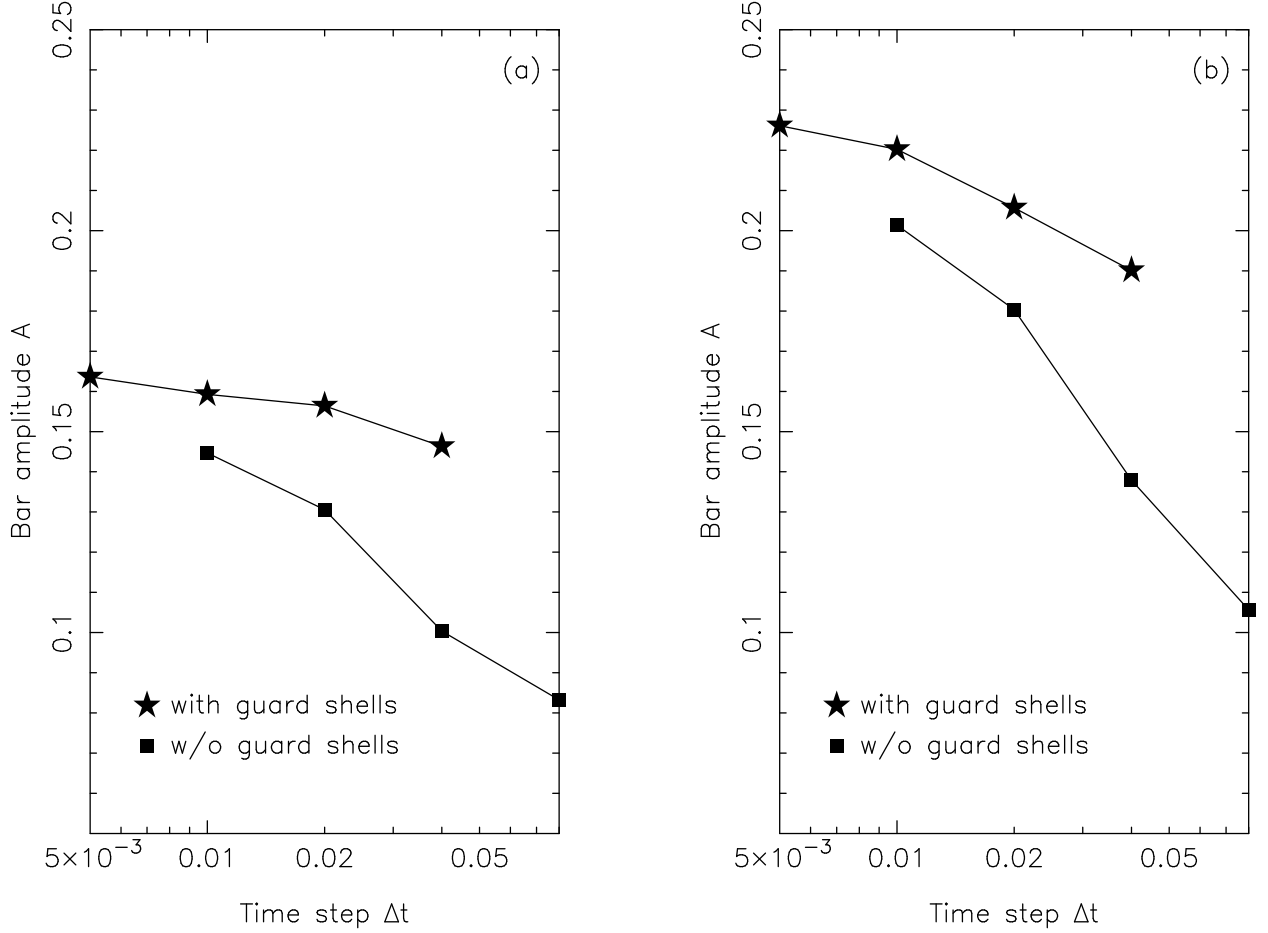
Fig. 7.— The bar amplitude A, measured at some fixed time after t_{grow}, as a function of the adopted time step Δt, for the weak initial bar (a) and strong initial bar (b), with all other parameters held fixed. The stars and squares show, respectively, results from runs with and without the guard shells scheme. The final amplitude decreases rapidly as longer time steps are employed. Special care, such as our guard shells scheme, is needed to obtain the correct final amplitude when a massive hard CMC is introduced.
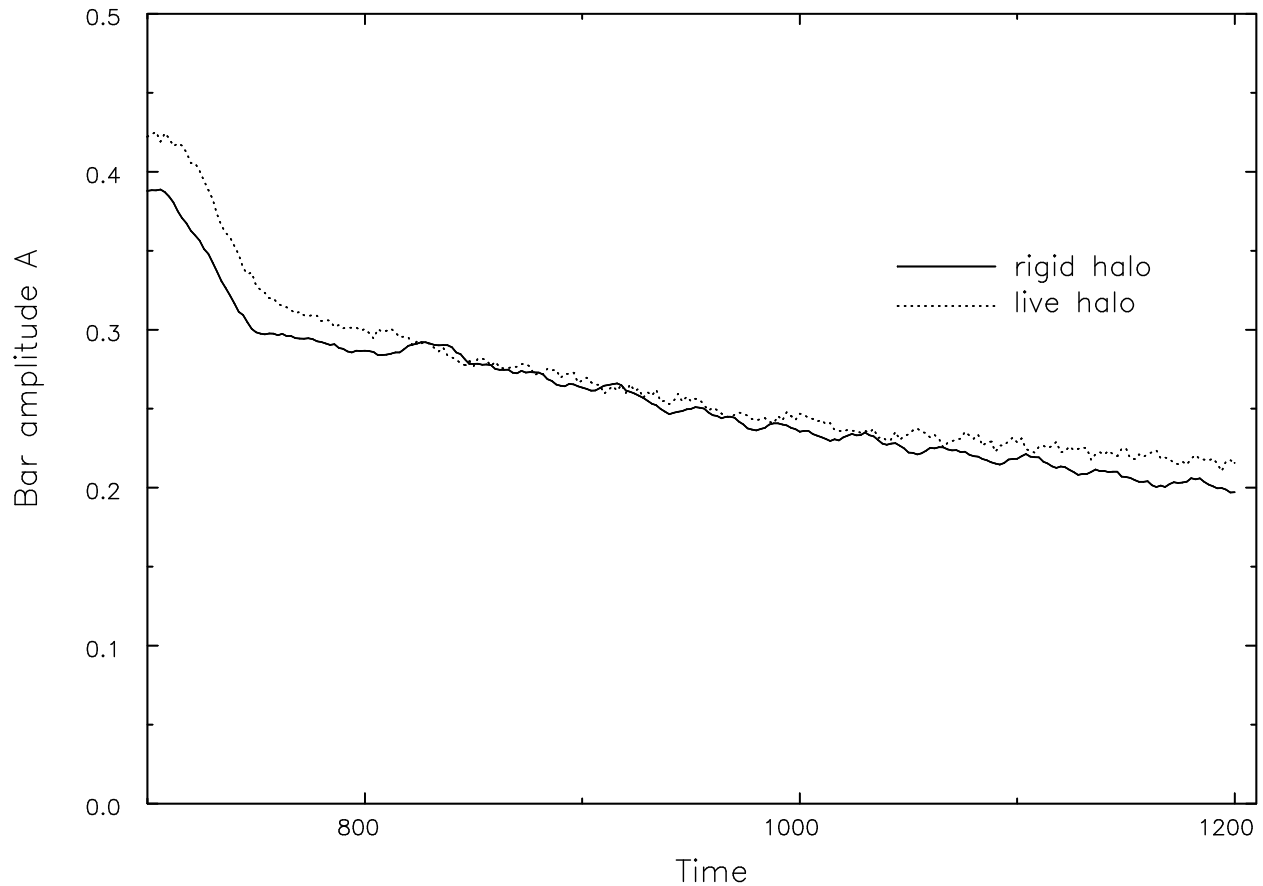
Fig. 8.— Comparison between runs using a rigid and a live halo for the nearly same halo potential. The two runs have the same CMC parameters ($M_{\mathrm{CMC}} = 0.02 M_{\mathrm{d}}$, $\epsilon_{\mathrm{CMC}} = 0.003$ and $t_{\mathrm{grow}} = 50$). Note that the bar amplitudes differ slightly at the start. The similarity the two results suggests that a rigid halo is an adequate approximation, at least for the large-core halo described in Eq. (4).
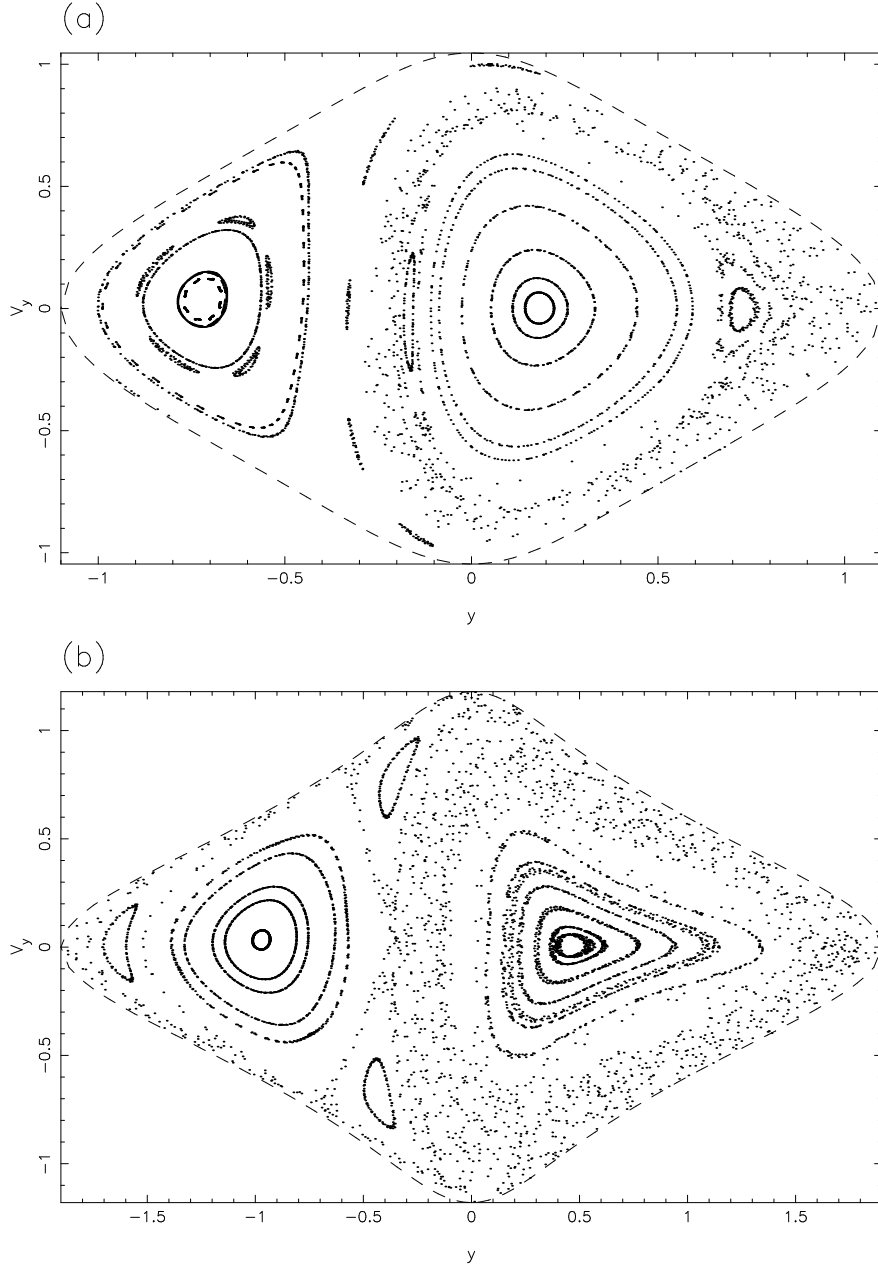
Fig. 9.— Surfaces of section at two energies for a case with no central mass. Many different test particle orbits of the chosen energy contribute to each plot, which is constructed from the gravitational field in the simulation at t=700. The dashed curve shows the zero-velocity curve (i.e. the boundary of the region energetically accessible) for the energy specified by the limiting distance, y_{max}, that a particle may reach on the bar minor axis. (a) SOS for $y_{max} = 1.1$ ($E_J = -0.5683$) and (b) for $y_{max} = 1.9$ ($E_J = -0.4196$).
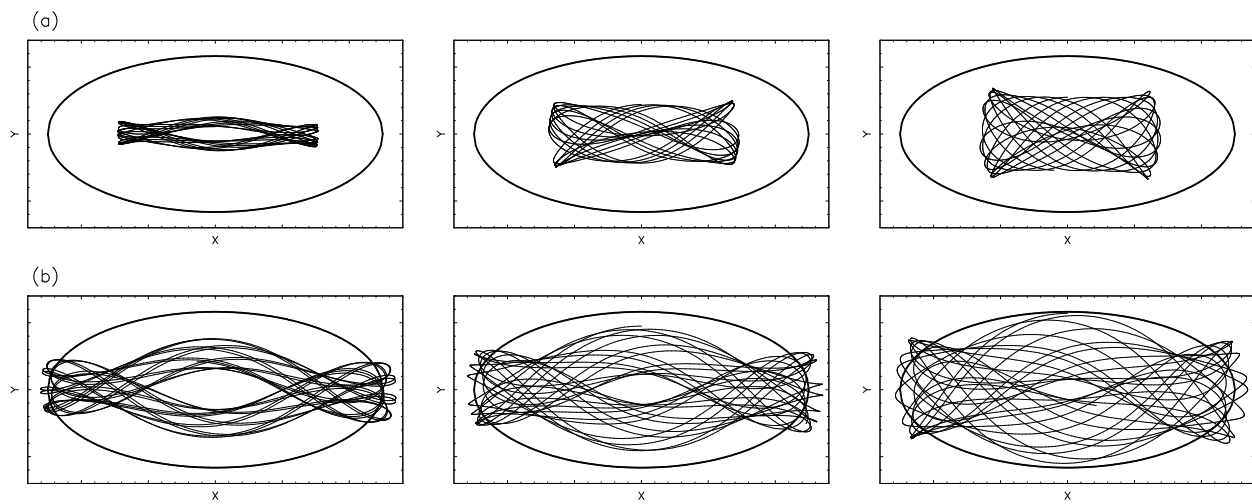
Fig. 10.— Sample x_1 orbits (in the $z = 0$ plane) viewed in a frame corotating with the bar. The top row (a) have E_J of the SOS Figure 9(a), while the bottom row (b) have the higher E_J of Figure 9(b). The ellipse in each panel is the bar outline for t=700 shown in Figure 1(b).
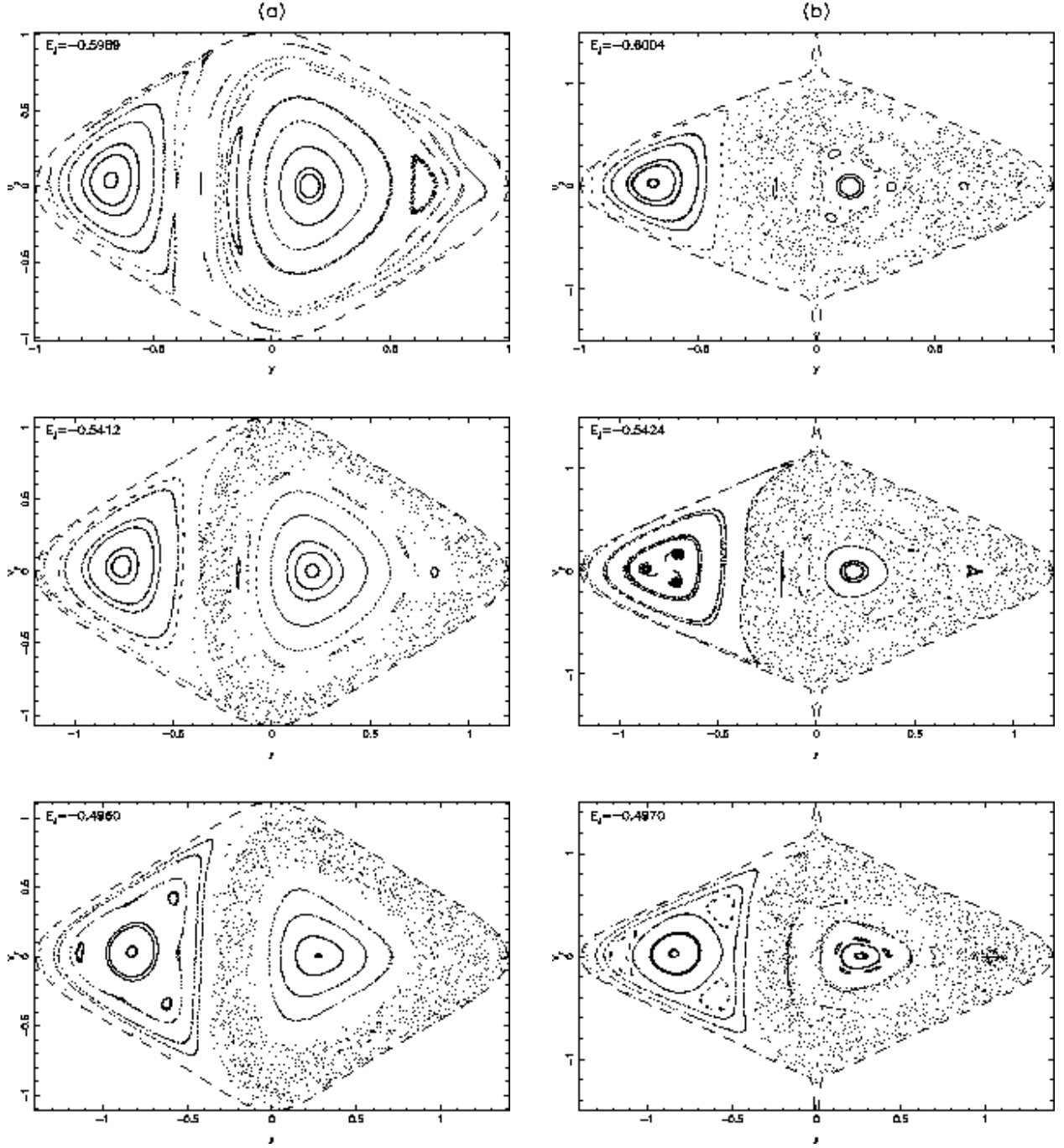
Fig. 11.— The evolution of SOSs for $y_{\max}$= 1.0, 1.2 and 1.4 (from top to bottom) after a hard CMC ($\epsilon_{\mathrm{CMC}} = 0.001$, $M_{\mathrm{CMC}} = 0.02M_{\mathrm{d}}$) is grown from $t = 700$ to 750. Column (a) shows the SOSs at $t = 700$, just before the CMC is added. Columns (b) to (f) show the SOS at the same values of $y_{\max}$ at times 710, 720, 730, 740 & 750 respectively.
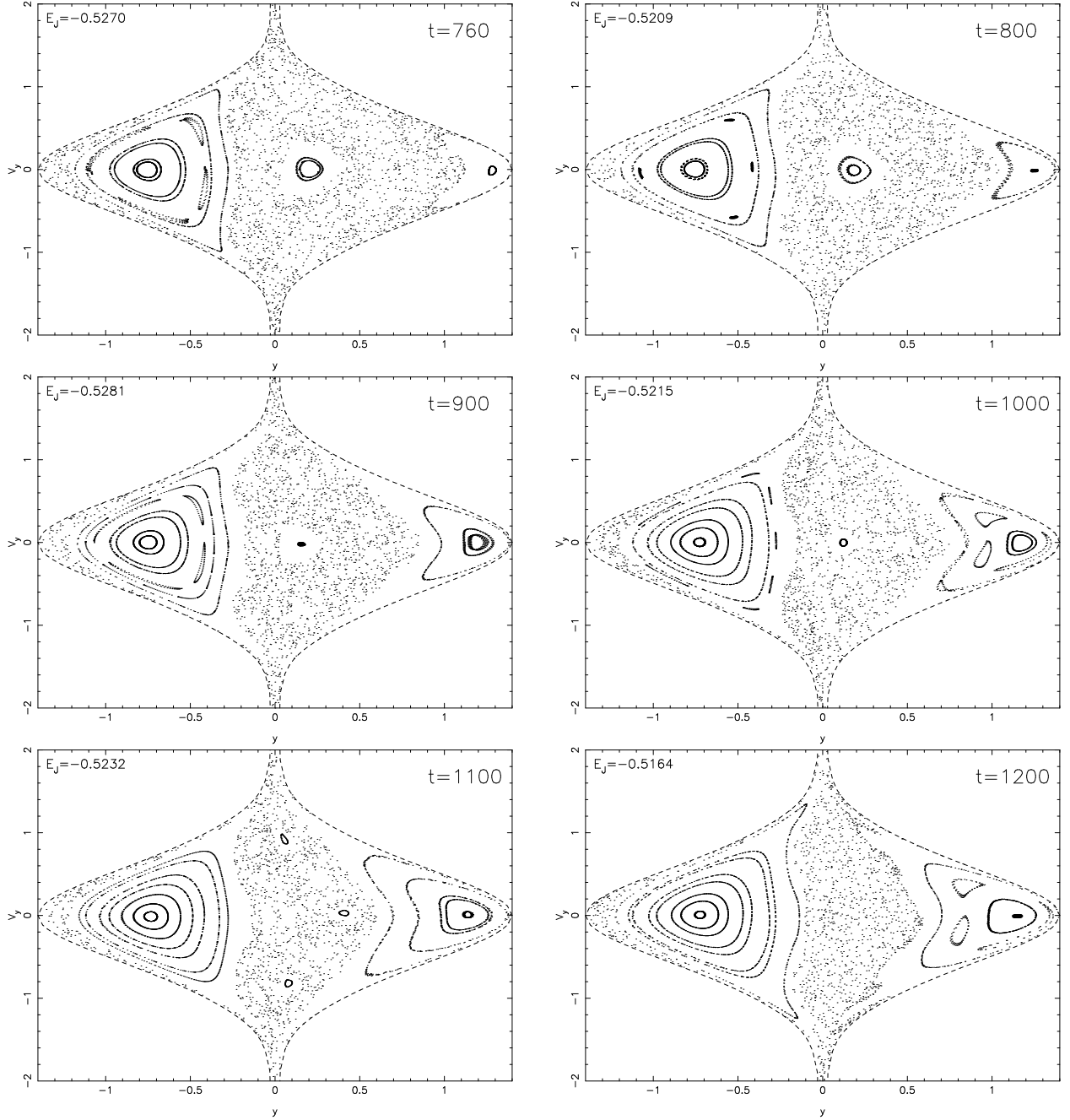
Fig. 11.— (c) & (d)

(e)

(f)
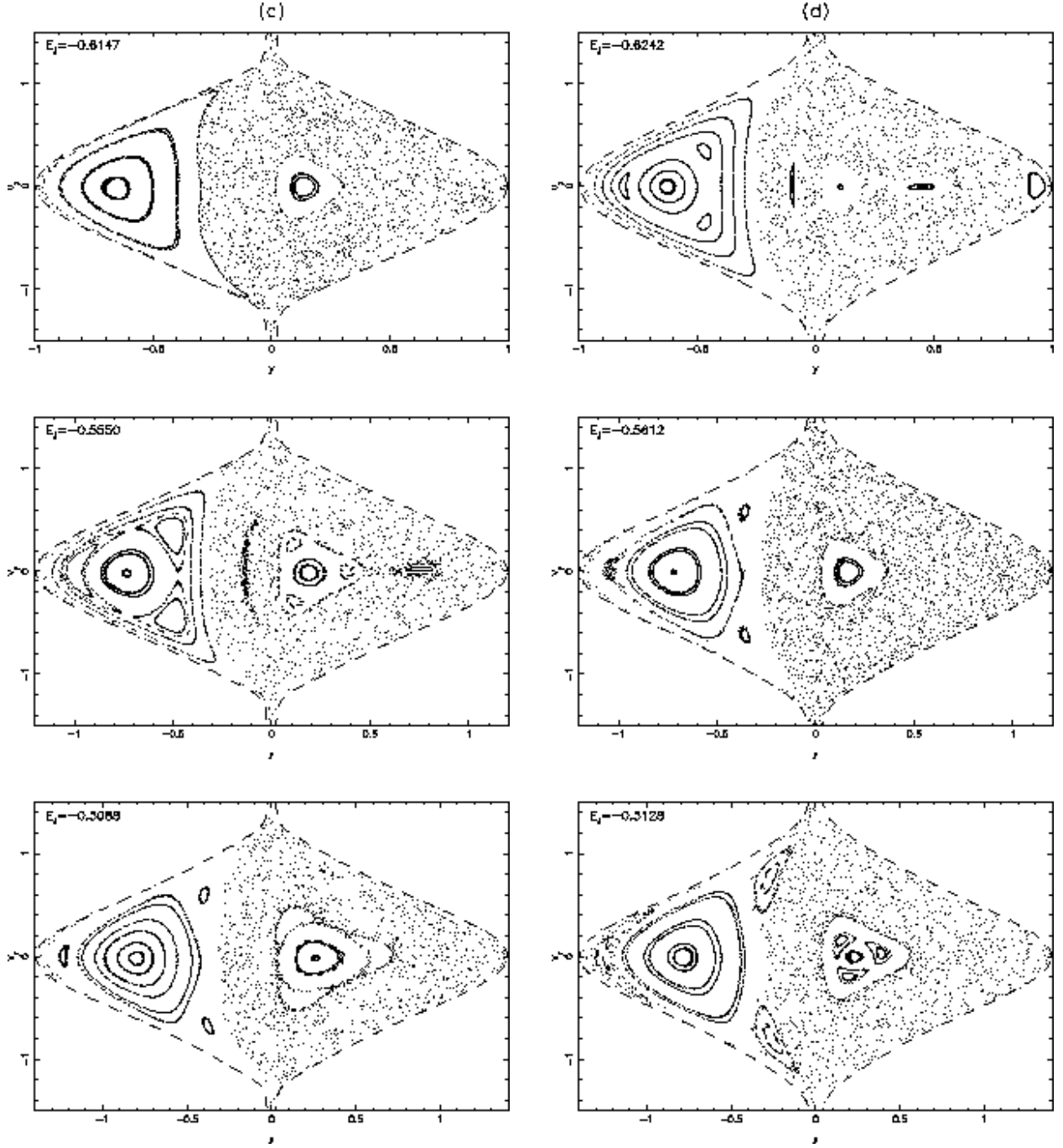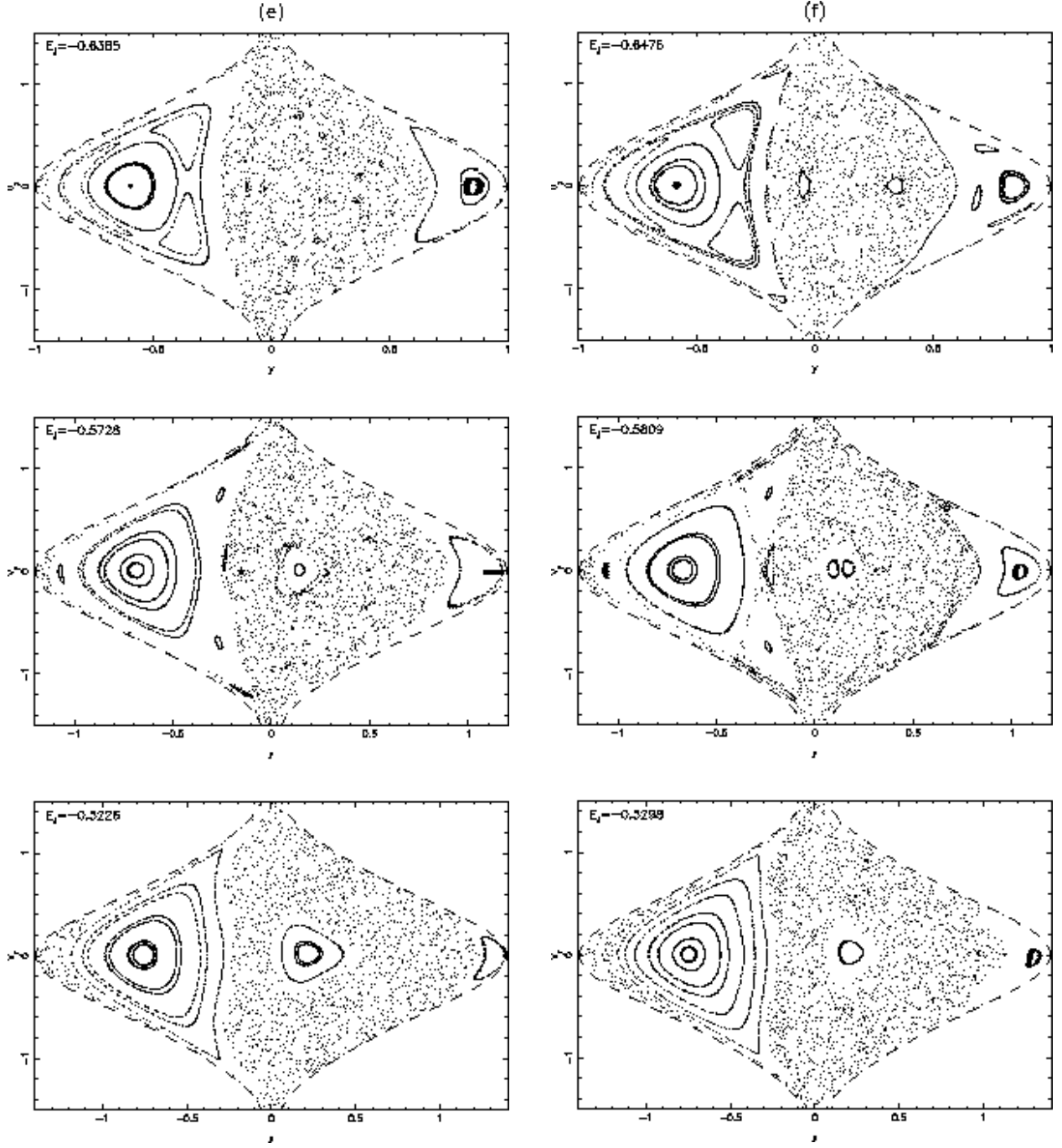
Fig. 11.— (e) & (f)

Fig. 12.— The time evolution of the SOS for $y_{\max} = 1.4$ after the CMC has reached its final mass. The corresponding time for each SOS is shown on the upper-right corner of each panel. The regular region of the bar-supporting x_1 orbit family gradually diminishes at this energy, consistent with the on-going decay of bar strength after t_{grow}.
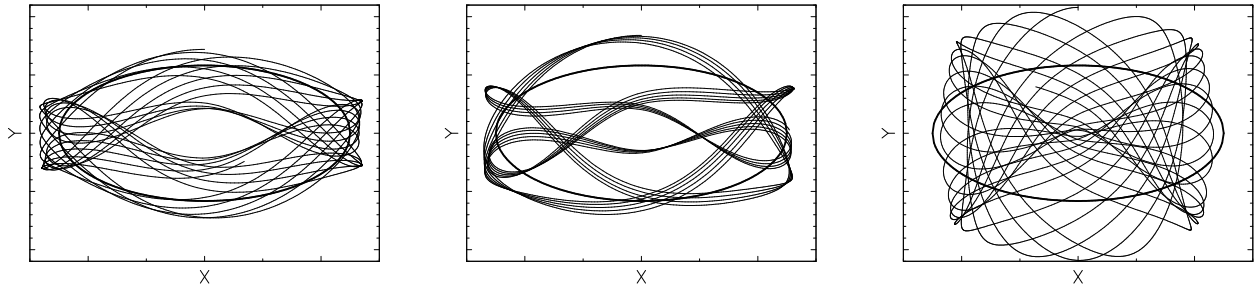
Fig. 13.— Three x_1 orbits (in the $z = 0$ plane) with the same high $E_J = -0.3874$, for the model at $t = 1100$, showing that fatter x_1 orbits are favored at late times. The ellipse in each panel is the outline of the initial bar at $t = 700$.
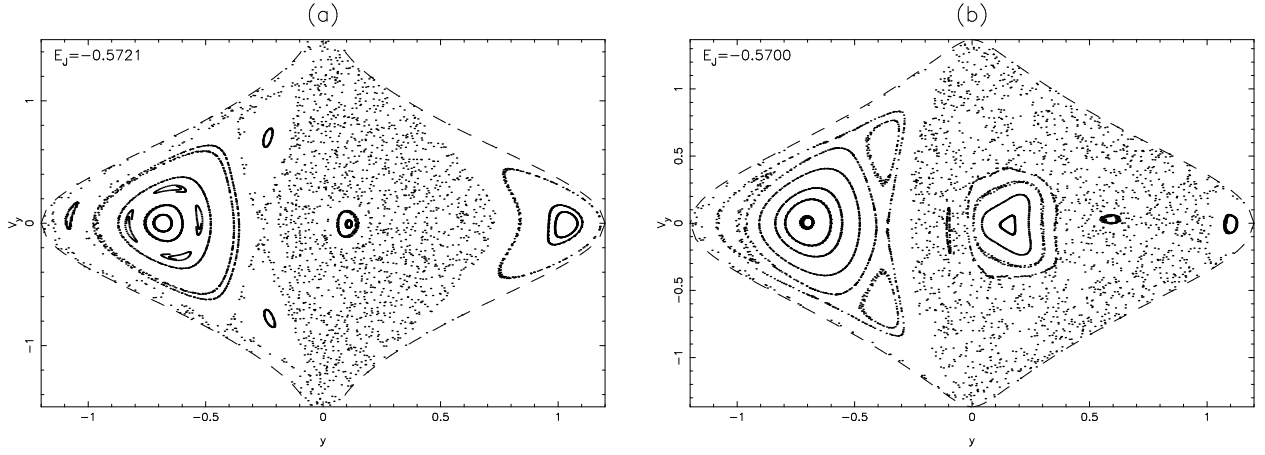
Fig. 14.— Comparison of SOS (y_{max}= 1.2) at $t = 800$ for the fiducial run with a hard CMC ($\epsilon_{\mathrm{CMC}} = 0.001$) on the left (a), and for a similar case with a soft CMC ($\epsilon_{\mathrm{CMC}} = 0.1$) on the right (b).
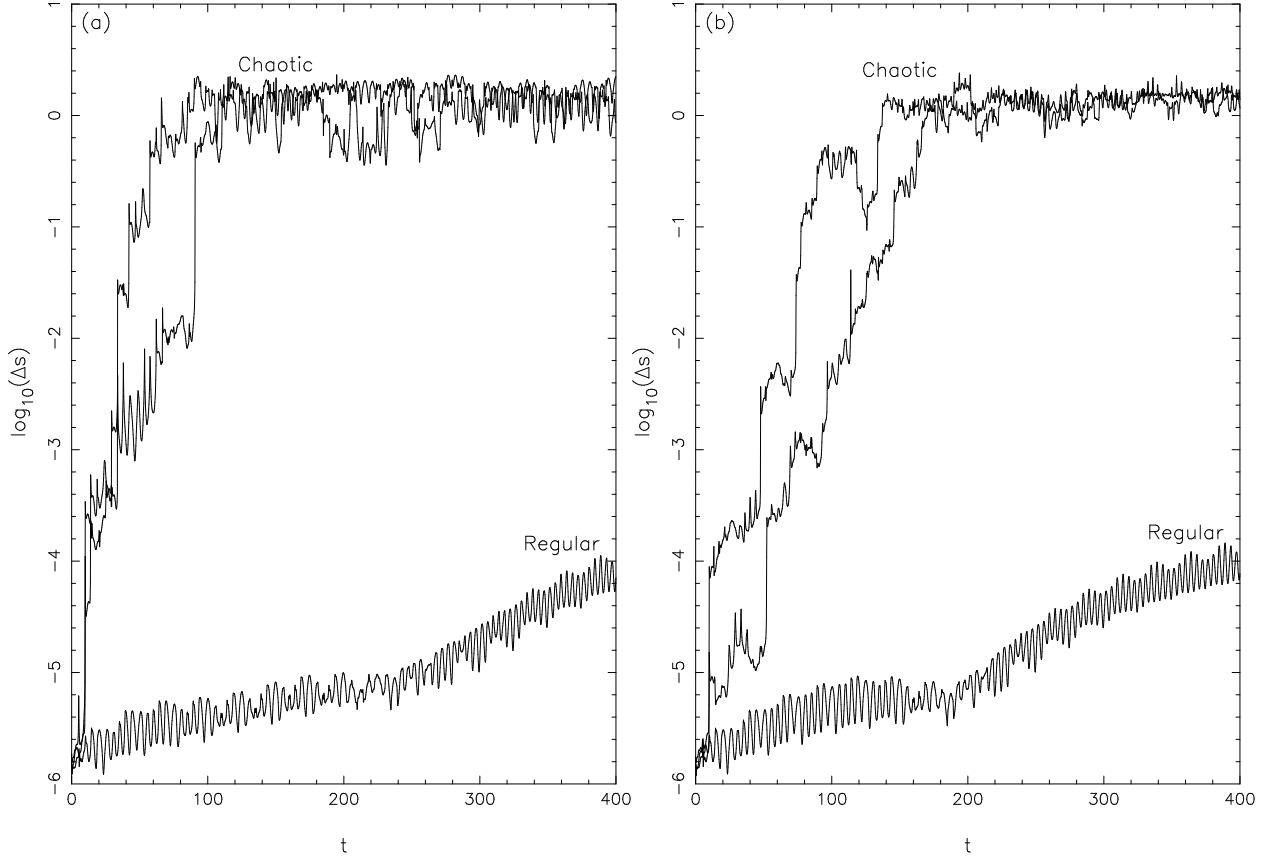
Fig. 15.— The time evolution ($\sim$ 5 Gyr) of phase space separation due to a infinitesimal perturbation for the potential at $t = 740$, $E_J = -0.6385$. (a) 2-D case: orbits are confined to the $z = 0$ midplane. The corresponding 2-D SOS plot is the top panel of Figure 11(e). From top to bottom for both panels, the three curves correspond to initial y=0.2, 0.5 and 0.8, respectively. (b). as for (a), but in this case full 3-D motion is allowed.
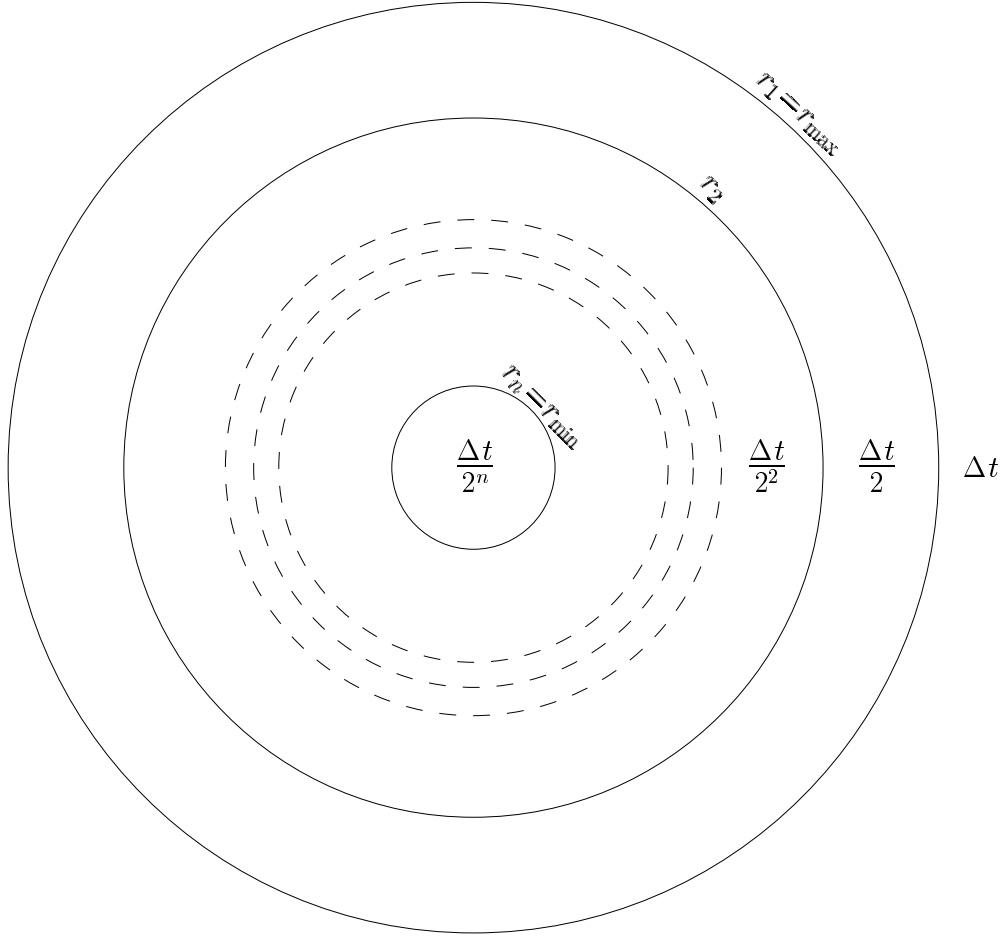
Fig. 16.— A sketch (not to scale) of n guard shells around a compact central mass (not shown). The ratio of the adjacent radii is $r_{i+1}/r_i = (1/2)^{2/3} \approx 0.63$.